The Astrophysical Journal, 763:32 (20pp), 2013 January 20 doi:10.1088/0004-637X/763/1/32

PROBING THE OUTER GALACTIC HALO WITH RR LYRAE FROM THE CATALINA SURVEYS

A. J. Drake[1], M. Catelan[2,3], S. G. Djorgovski[1], G. Torrealba[2], M. J. Graham[1], V. Belokurov[4], S. E. Koposov[4], A. Mahabal[1], J. L. Prieto[5], C. Donalek[1], R. Williams[1], S. Larson[6], E. Christensen[6], and E. Beshore[6]
[1] Department of Astronomy and the Center for Advanced Computing Research, California Institute of Technology, 1200 East California Boulevard, CA 91225, USA
[2] Departamento de Astronomía y Astrofísica, Facultad de Física, Pontificia Universidad Católica de Chile, Av. Vicuña Mackena 4860, 782-0436 Macul, Santiago, Chile
[3] The Milky Way Millennium Nucleus, Av. Vicuña Mackenna 4860, 782-0436 Macul, Santiago, Chile
[4] Institute of Astronomy, Madingley Road, Cambridge CB3 0HA, UK
[5] Department of Astronomy, Princeton University, 4 Ivy Ln, Princeton, NJ 08544, USA
[6] Department of Planetary Sciences, Lunar and Planetary Laboratory, The University of Arizona, 1629 East University Boulevard, Tucson, AZ 85721, USA
Received 2012 August 22; accepted 2012 November 9; published 2013 January 2

ABSTRACT

We present analysis of 12,227 type-ab RR Lyraes (RRLs) found among the 200 million public light curves in Catalina Surveys Data Release 1. These stars span the largest volume of the Milky Way ever surveyed with RRLs, covering ∼20,000 deg^2 of the sky ($0^\circ < \alpha < 360^\circ$, $-22^\circ < \delta < 65^\circ$) to heliocentric distances of up to 60 kpc. Each of the RRLs is observed between 60 and 419 times over a six-year period. Using period finding and Fourier fitting techniques we determine periods and apparent magnitudes for each source. We find that the periods are generally accurate to $\sigma = 0.002\%$ in comparison to 2842 previously known RRLs and 100 RRLs observed in overlapping survey fields. We photometrically calibrate the light curves using 445 Landolt standard stars and show that the resulting magnitudes are accurate to ∼0.05 mag using Sloan Digital Sky Survey (SDSS) data for ∼1000 blue horizontal branch stars and 7788 RRLs. By combining Catalina photometry with SDSS spectroscopy, we analyze the radial velocity and metallicity distributions for >1500 of the RRLs. Using the accurate distances derived for the RRLs, we show the paths of the Sagittarius tidal streams crossing the sky at heliocentric distances from 20 to 60 kpc. By selecting samples of Galactic halo RRLs, we compare their velocity, metallicity, and distance with predictions from a recent detailed *N*-body model of the Sagittarius system. We find that there are some significant differences between the distances and structures predicted and our observations.

Key words: galaxies: stellar content – Galaxy: formation – Galaxy: stellar content – Galaxy: structure – stars: variables: RR Lyrae

Online-only material: color figures, machine-readable tables

1. INTRODUCTION

The study of the formation of the Milky Way is fundamental to the understanding of our Galactic environment as well as that of galaxies in general. The past competing ideas of halo formation through monolithic collapse (Eggen et al. 1962) and through the accretion of protogalactic fragments (Searle & Zinn 1978) have largely been replaced by a combination of the two scenarios within the theory of hierarchical structure formation (e.g., Freeman & Bland-Hawthorn 2002).

The study of Galactic structure has continued to flourish in recent years with the discoveries of numerous tidal streams and dwarf galaxies within the Galactic halo (e.g., Majewski et al. 2003; Belokurov et al. 2006; Newberg et al. 2002). The most well-studied of these structures is the accretion of the Sagittarius dwarf galaxy (Sgr; Ibata et al. 1994). To date the Sgr stream has been traced on large scales using blue horizontal branch (BHB) stars (Newberg et al. 2003; Belokurov et al. 2006) and M giants (Majewski et al. 2003) with portions of the stream being studied using RR Lyrae (RRL; Vivas & Zinn 2006; Miceli et al. 2008; Sesar et al. 2010). In addition to the Sgr stream, there is also evidence for a Virgo stellar stream (VSS; Vivas & Zinn 2006; Vivas et al. 2008) using RRLs and a Virgo overdensity (VOD; Newberg et al. 2002) from F-type main-sequence stars (Newberg et al. 2007). An overdensity in Pisces was reported by Sesar et al. (2007) and confirmed by Kollmeier et al. (2009). A Monoceros stream has also been discovered (Newberg et al. 2002; Majewski et al. 2003) that may be due to the disruption of the putative Canis Major dwarf (Casetti-Dinescu et al. 2006), although the existence of this structure remains uncertain (Momany et al. 2004; Mateu et al. 2009). In addition, a Cetus stream has been discovered in the south (Newberg et al. 2009; Koposov et al. 2012) and Belokurov et al. (2007) also note that the presence of an overdensity of BHB stars dubbed the Hercules-Aquila cloud.

Although the number of streams and structures found in the outer Galactic halo (galactocentric distances >15 kpc) has significantly increased in the past 10 years, numbers fall far short of the hundreds predicted by ΛCDM models of hierarchical structure formation (e.g., Bullock et al. 2001; Freeman & Bland-Hawthorn 2002). This "missing satellite" problem (e.g., Bullock et al. 2001) continues to be important to our understanding of galaxy formation and requires us to probe the Galactic halo to distances well beyond 20 kpc.

RRLs are fundamental distance probes that can be used to trace the history of galaxy formation (e.g., Catelan 2009, and references therein). To date a few tens of thousands of RRLs are known in dense regions near the Galactic bulge, where the Sgr dwarf galaxy is located. Similar numbers of RRLs are known also in the Magellanic Clouds, again thanks to microlensing surveys toward dense stellar fields (Soszyński et al. 2009; Pietrukowicz et al. 2012). However, the Galactic halo itself has only been probed with confirmed RRLs over a few thousand

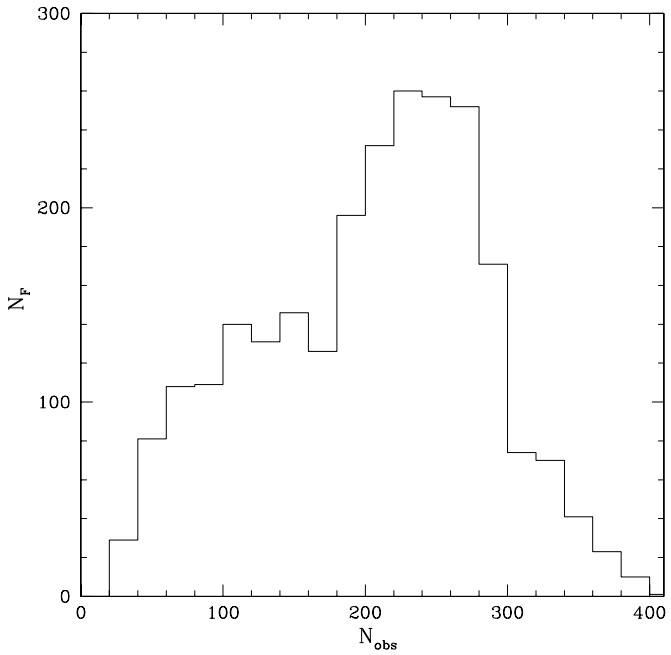

Figure 1. Distribution of the number of CSS image fields (N_F) having specified numbers of observations (N_{obs}).

square degrees to heliocentric distances of ∼30 to 100 kpc (e.g., Vivas et al. 2004; Keller et al. 2008; Miceli et al. 2008; Watkins et al. 2009; Sesar et al. 2010). In this paper we outline our search, discovery, and calibration of the RRLs to ∼50 kpc. We then undertake a preliminary analysis of the structures uncovered.

2. OBSERVATIONAL DATA

The Catalina Sky Survey[7] began in 2004 and uses three telescopes to cover the sky between declination $\delta = -75°$ and +65° in order to discover near-Earth objects (NEOs) and potential hazardous asteroids (PHAs). Each of the survey telescopes is run as separate sub-surveys. These consist of the Catalina Schmidt Survey (CSS) and the Mount Lemmon Survey (MLS) in Tucson Arizona, and the Siding Spring Survey (SSS) in Siding Spring, Australia. In general, each telescope avoids the Galactic plane region by between 10° and 15° due to reduced source recovery in crowded stellar regions. All images are taken unfiltered to maximize throughput. Photometry of all images is carried out using the aperture photometry program SExtractor (Bertin & Arnouts 1996). In addition to asteroids, all the Catalina data is analyzed for transient sources by the Catalina Real-time Transient Survey (CRTS; Drake et al. 2009; Djorgovski et al. 2011).

In this paper, we concentrate on the data taken by the CSS 0.7 m telescope between 2005 April and 2011 June. These data cover 20,155 deg^2 in the region $0° < \alpha < 360°$ and $-22° < \delta < 65°$. For this CSS telescope each image from the 4k × 4k Catalina CCD camera covers 8 deg^2 on the sky. All these archival observations analyzed in this work were taken during spans of 21 nights per lunation in sets of four images separated by 10 minutes. The exposure times are typically 30 s and reach objects to $V = 20$ mag, depending on seeing and sky brightness. The distribution of observations in the CSS fields is given in Figure 1.

[7] http://www.lpl.arizona.edu/css/

3. CALIBRATION

In order to use RRLs as probes for distances it is necessary to accurately calibrate the observed magnitudes to a standard system. All observations are transformed to Johnson V based on 50–100 stars selected as G-type stars using Two Micron All Sky Survey (2MASS; Skrutskie et al. 2006) colors. For bright stars, this photometry provides repeated photometry accurate to ∼0.05 (Larson et al. 2003). However, as the photometry is unfiltered there are significant variations with object color. The first step to determining accurate distance is calibration of the color terms required, thus placing the photometry on a standard system.

The Landolt (2007) *UBVRI* standard star catalog provides 109 stars centered near declination −50° in the magnitude range $10.4 < V < 15.5$ and in the color index range $-0.33 < (B - V) < 1.66$, while Landolt (2009) provides a catalog of 202 standard stars along the celestial equator in the magnitude range $8.90 < V < 16.30$, and the color index range $-0.35 < (B - V) < 2.30$, along with 393 standard stars from previous standard star catalogs.

For photometric calibration, we combine observations taken with all three Catalina Sky Survey telescopes since no difference was found between these systems. This is not surprising since each telescope specifically uses the same type 4k × 4k CCD camera and observations with all three telescopes are calibrated using the same software pipeline. In total there are 445 Catalina light curves matching Landolt standards. On average each standard is measured 134 times. To reduce sources of error we first determined the variability index of each light curve. We remove a handful of stars that appeared to exhibit significant variability. As noted by Landolt (2009), this catalog includes a small number of known variable stars.

In order to compare CSS V magnitudes to Landolt values, we first determined median magnitudes for each light curve and calculated the difference from the standard value. In Figure 2, we plot the difference between Landolt standards and transformed median CSS magnitudes. The high degree of scatter is due to the clear difference between the transformed unfiltered observations and filtered observations. The Landolt data set contains values for U, B, V, R, and I filters. To better calibrate the photometry we fit the differences with the various possible color terms. The color transformations were clearly nonlinear. We find the following transformations:

$$V = V_{\rm CSS} + 0.31 \times (B - V)^2 + 0.04, \quad (1)$$

$$V = V_{\rm CSS} + 0.91 \times (V - R)^2 + 0.04, \quad (2)$$

$$V = V_{\rm CSS} + 1.07 \times (V - I)^2 + 0.04. \quad (3)$$

In Figure 2, we also plot the difference in magnitudes after applying this calibration. The dispersion in the fits to these transformations are 0.059, 0.056, and 0.063 mag, respectively, for $V < 16$.

The average $B - V$ color of RRL is about 0.3 mag with stars varying between about 0.1 and 0.5 as they pulsate (Nemec 2004). For most of our sample we have no color information, so we adopt the average color. From Equation (1), this leads to a correction of 0.028 mag. From the transformations the range of possible colors gives rise to a maximum uncertainty of ∼0.07 mag in V. Combining this with the photometric uncertainty, we expect a dispersion of $\sigma = 0.09$ mag in our RRL photometry. However, based on random phase Sloan Digital

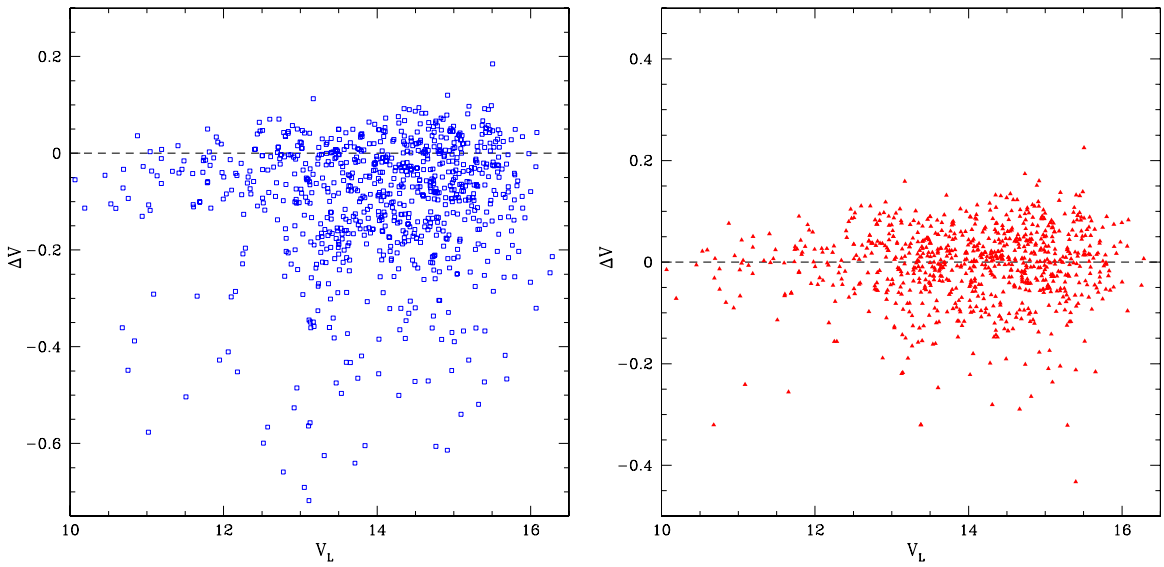

Figure 2. Comparison of CSS *V* magnitudes with Landolt magnitudes for standard stars. The left plot shows the difference in magnitudes before color corrections and the right plot shows the difference after color corrections have been applied.

(A color version of this figure is available in the online journal.)

Sky Survey (SDSS) photometry, we will show that the RRLs in our sample are strongly concentrated in a color index range of 0.1 mag. Further tests of the importance of RRL color variations in CSS data were carried out by G. Torrealba et al. (in preparation) and found to be unimportant.

To determine the photometric accuracy of the calibration at fainter magnitudes than Landolt standards we selected the sample of 1170 BHB stars of Sirko et al. (2004). These stars have similar ages, masses, and $(u-g)$ colors to RRL stars. However, they have significantly different $(g-r)$ colors (centered near -0.2, compared to +0.2 for the RRLs). We matched the BHB source locations with CSS objects and removed 93 sources that matched candidate or known variable stars. As we want to determine robust estimates, we also removed objects with fewer than 20 CSS observations. The average number of measurements for the remaining 1026 BHB stars was 223. We transformed the SDSS DR8 photometry for the source to *V* using the Lupton[8] 2005 transformation equations. For each source we determined median CSS *V* magnitudes using Equation (1) and $B-V$ colors from SDSS data. In Figure 3, we plot the difference between *V* magnitudes derived from SDSS and CSS and by binning the difference in 1 mag bins we also show how the scatter increases with decreasing source brightness.

Of the 1026 BHB stars, 14 had offsets >0.3 mag. Nine of these objects were found to be blended in the CSS photometry (but not in SDSS photometry). For the remaining objects we find an average difference of 0.0065 mag and $\sigma = 0.065$. As expected, the level of variation increases with decreasing brightness. Considering that these stars are much fainter than the Landolt standards the level of agreement is very good.

4. SAMPLE SELECTION

The Catalina Surveys Data Release 1 (CSDR1) covers 198 million discrete sources ranging in *V* from 12 to 20 with an average of 250 observations per location. In order to discover the RRLs among these sources, we first calculate the Welch–Stetson variability index I_{WS} (Welch & Stetson 1993) for every source.

[8] http://www.sdss.org/dr5/algorithms/sdssUBVRITransform.html

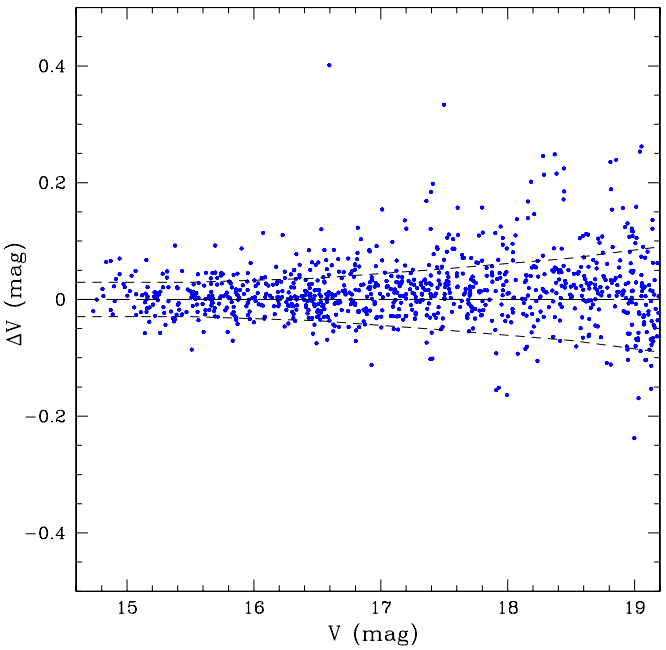

Figure 3. Comparison between SDSS and CSS magnitudes transformed to *V* for ∼1000 BHB stars selected by Sirko et al. (2004). The long-dashed line marks the expected zero-offset line. The short-dashed lines show the 1σ uncertainties.

(A color version of this figure is available in the online journal.)

Based on initial investigation we selected sources with $I_{WS} > 0.6$ as possible variables. For sources brighter than $V = 13.25$ we set a higher variability threshold due to saturation effects. We also only selected light curves with more than 40 points. This process returned 8.7 million potential variable sources, or 4.4% of the sources. Every candidate variable source was then checked for periodicity using the Lomb–Scargle (LS; Lomb 1976; Scargle 1982) periodogram analysis. This method was chosen since it was found to take approximately a second per light curve, compared to between 10 s and a few minutes for other techniques. Periodic sources were selected based on LS peak significance statistic p_0. This value represents the probability that the observed signal was observed purely due

to chance fluctuations. However, we note that care must be taken when interpreting these values (Schwarzenberg-Czerny 1998). Objects with very small values, $p_0 < 10^{-7}$, were chosen as good candidate periodic variables after the inspection of a few hundred sources phased to their best LS periods. Based on the CSS light curves of known periodic variables, M. J. Graham et al. (in preparation) found that this technique gives the correct periods for ≈83% of known RRab's with this sampling. An additional 13% of the RRLs were detected as significantly periodic, yet the period did not match the known period.

Of the variable sources, 375,000 were found to exhibit periodicity at our significance level. However, a very large fraction of the periods were found to be spurious detections near 0.5 and 1 days. These periods are purely due to the observing cadence of CSS. Upon close examination of the period distribution we removed all candidates with periods in the ranges 0.497 days $< P <$ 0.501 days or 0.994 days $< P <$ 1.0035 days. Additional period aliases were found within individual fields. In these cases, systematics were found to lead to the detection of many sources with very similar periods. We also removed periodic variable candidates where three or more sources within a given field had the same periods to <0.2%. These cuts are expected to remove a very small fraction of the RRL with periods within these ranges.

To obtain a clean sample of RRL appropriate for distance determinations we decided to use only type-ab RRL (RRab), since c-type (RRc) and d-type (RRd) light curves are often very similar to W UMa type eclipsing binary light curves that occur in the same period region. For example, some past surveys have misidentified W UMa sources as RRc's (Kinman & Brown 2010). W UMa stars are more common than RRc variables, so even though most can be distinguished in well-sampled data, including RRc's is likely to lead to some contamination.

Among the periodic sources we initially selected objects with periods between 0.36 and 1.4 days to conservatively include all RRab's found at their true period, as well as many of those found at aliases of their period in the LS analysis. A total of 23,346 objects were found in this period range. From the phased light curves, a large number of these sources were clearly eclipsing binaries of all types, as well as RRc's found at aliases of their true periods.

To recover the 13% of sources that we expect to be detected at an incorrect period, and to determine more accurate periods among the periodic candidates, we determine the 10 best periods for each source using the Analysis of Variance (AoV) program (Schwarzenberg-Czerny 1989). The AoV program was run in two stages which each provided five periods. First, the software was run in the normal *AoV-mode* and then with the multi-harmonic method (Schwarzenberg-Czerny 1996). We compare these periods to the five best values found using the LS technique, giving us a total of 15 test periods. As there were many cases where the most significant period found by each method did not match that given by others, further analysis was undertaken.

To select the correct period for each object we follow the Adaptive Fourier Decomposition (AFD) method (G. Torrealba et al., in preparation). Here the phased light curves were fit with an increasing series of Fourier harmonics using a weighted least-squares technique. The order of the harmonic fit is chosen by determining whether the improvement in the observed reduced χ^2 with addition of higher-order terms is statistically significant based on the statistical F-test. This is evaluated by determining the likelihood of observing the improvement in reduced χ^2 given

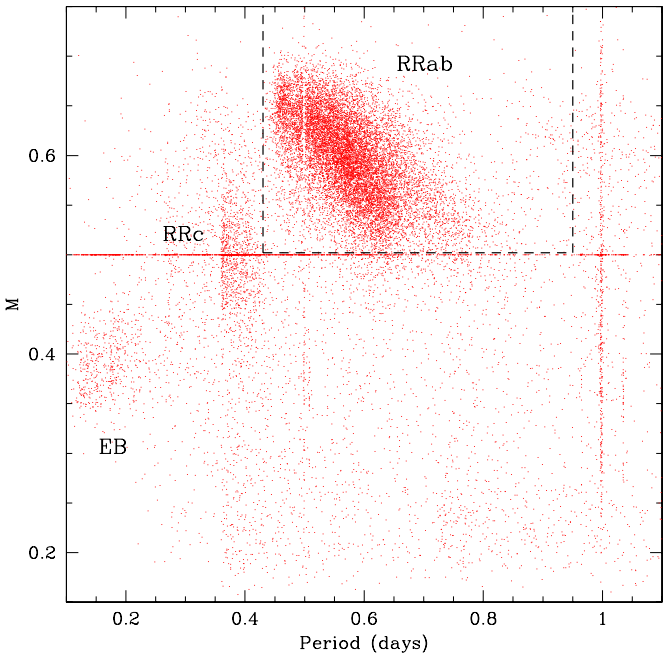

Figure 4. Values of the Kinemuchi et al. (2006) M-test statistic used to select RRab's from other period variables. The dashed line shows the border of the period region selected in this work.

(A color version of this figure is available in the online journal.)

the number of parameters and avoids overfitting the data with a single high-order series. In addition, since RRab's require more Fourier terms to fit than most eclipsing binaries and RRc's, the fit order also provides additional discrimination between variable star types.

We produced phase-folded light curves using the 15 most significant periods from AoV and LS. These were fit to select the best period based on their reduced χ^2 values. In addition, to minimize the influence of bad data, each object is refit successively after removing outliers 3σ from the original fits. For RRab selection we remove sources where the best fit to the phased light curves is sinusoidal. This is done by only selecting objects where the best Fourier fit is of the order of three and above. Objects with large reduced χ^2 values at all periods were removed from the candidate list.

To further separate the RRab from W UMa variables we select only objects where the best-fit period among the 15 candidates is between 0.43 and 0.95 days. For the remaining set we apply the M-test (Kinemuchi et al. 2006, their Equation (8)). This test statistic measures the fraction of time that an object spends below the mean magnitude. Light curves with $M > 0.502$ are selected as RRab's since these sources spend most of the time above their average magnitude. In Figure 4, we show the best-fit periods of all the sources and their M-test values. The dashed lines show the region where RRab sources are selected. Light curves with $M = 0.5$ are sinusoidal W UMa and RRc variables. The eclipsing binaries are mainly concentrated at short periods near 0.2 days since these sources are very often found at half their true period. The RRc's are seen near 0.4 days but, as already explained, they are likely contaminated by some eclipsing binaries. The cutoff seen near 0.35 days and the slight gap near 0.5 days are due to the initial period selection limits. Many objects are seen near 1 day due to the daily sampling-rate alias. Of the initial selection, 12,471 are selected as RRab stars.

In Figure 5, we plot the period–amplitude distribution of CSS RRab's. In the right panel of this figure, we also present a Hess

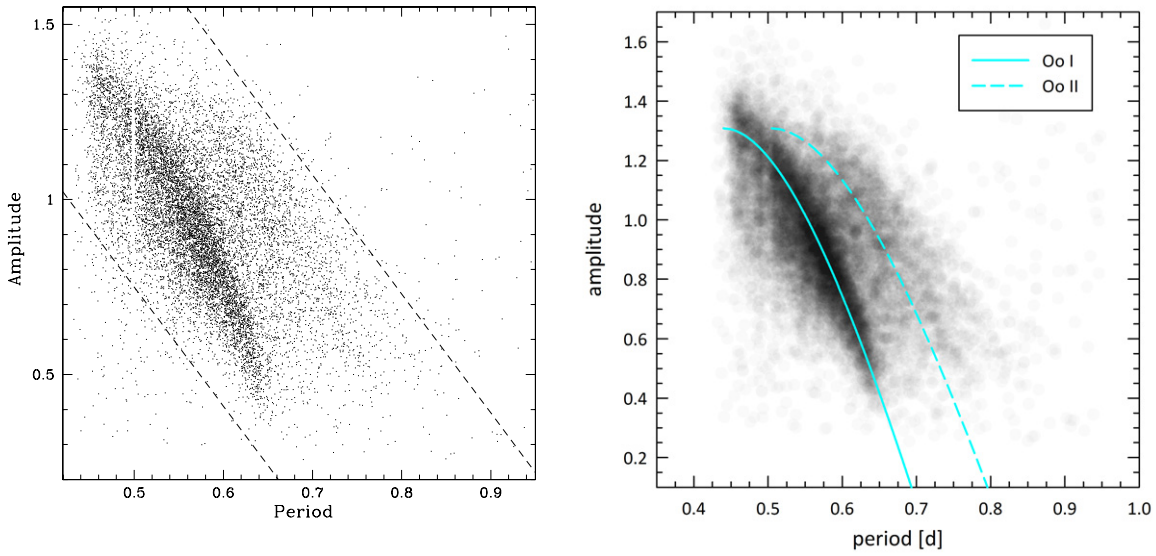

Figure 5. Period–amplitude diagram (aka "Bailey diagram") for RRab's found in this work. In the left panel, the dashed lines presents the lower ($A > 2.3$–$3.4 \times P$) and upper ($A = 3.3$–$3.4 \times P$) limits expected for most of the RRab's. The RRab's near 0.5 days are missing since the selection procedure removes non-periodic sources occurring sampling aliases. In the right panel, we plot the Hess (point density) diagram with reference lines for OoI and OoII systems, based on Equation (11) in Zorotovic et al. (2010).

(A color version of this figure is available in the online journal.)

(relative density) diagram for this same data. This figure shows that almost all of the RRab's lie near the Oosterholf type-I (OoI) period–amplitude sequence. However, the amplitudes are slightly smaller than predicted since we have assumed average $B - V$ color, whereas RRab's vary in color with phase (Hardie 1955). From Equation (1), we find that a $B - V$ color variation, between $B - V = 0.1$ at maximum and $B - V = 0.5$ at minimum, would lead to a 0.08 mag increase in the V amplitude. In comparison with the RRab V amplitudes of Zorotovic et al. (2010), we find that the CSS RRab amplitudes are uniformly underestimated by 0.15 mag and correct for this factor.

A sequence of RRab's are seen at longer periods due primarily to lower-metallicity Oosterholf type-II (OoII) RRab's (e.g., Smith et al. 2011). However, the fraction of Oosterholf-II stars is far smaller than observed for a sample of 1455 nearby ($d < 4$ kpc) RRab's observed by Szczygiel et al. (2009). The figure exhibits the presence of a gap in the distribution near 0.5 days due to our period selection where we removed periods near sampling aliases. Based on the number of RRab's with slightly shorter and slightly longer periods, we estimate the number of stars in this range to be around 160 stars, or ∼1.3% of the total.

Using the OoI period–amplitude relation defined by Zorotovic et al. (2010) we determine period shifts for each RRab as shown in Figure 6. The result is remarkably similar to the one shown in Figure 20 of Miceli et al. (2008), and thus is consistent with OoI and OoII components being present in our data as well. The fit with two Gaussian components that is shown in the figure possesses a correlation coefficient $r = 0.985$ and a standard error of 25.4. We also fitted a skew-normal distribution to the data, based on Equation (3) of Azzalini (1985). The result is shown in Figure 6. This fit is noticeably worse than the two-Gaussian fit, with $r = 0.955$ and a standard error of the estimate of 43.3. This confirms that, as in the case of Miceli et al. (2008), our distribution is also comprised of two separate components, which are naturally interpreted as OoI and OoII. However, the OoII component is clearly smaller in our case; the two-Gaussian fit implies that around 76% of our stars belong to the OoI, and 24% to the OoII population. There is, in addition, a clear excess of stars toward negative period shifts, which can be plausibly ascribed to the presence of the Blazhko effect as well as RRab's that are blended with other sources.

We examined the phased light curves of all the objects outside the region bounded by the dashed lines in Figure 5. Of the 439 RRab candidates in these regions, 140 were discovered not to be RRab's and removed. Most of the objects removed were variable stars near the CSS saturation limit, $V \sim 12.5$. Many of the objects with unexpected amplitudes for an RRab were found to be blended sources. For close blends the additional flux tends to reduce the observed amplitude. For sources with slightly larger source separations the amplitude can actually increase slightly. In such cases, the flux from the two separate sources are detected individually at minimum. As the RRab's flux increases, the nearby source becomes merged with the RRab flux.

The average number of photometric measurements for the RRab candidates is 219, with the poorest sampled having 60 and the best sampled having 416 measurements. In Table 1, for each source we present the locations, average V magnitudes, periods, amplitudes, number of photometry measurements, distances, and extinction. In Figures 7 and 8, we present the locations of the RRab's discovered in CSS survey fields.

In Figure 9, we plot representative examples of RRab light curves spanning the range of discoveries from $V = 12.5$ to 19.5. Each light curve has been folded with the period we discovered. The figure shows that the brightest RRab, near mag 12.5, shows significant saturation effects. This will affect the fits for these sources. However, there are only 62 RRab's in our sample brighter than $V = 12.5$. A small fraction of the points shown in other light curves are clearly outliers caused by image artifacts and poor seeing. As outlined above, these points are removed during the period finding and Fourier fitting process.

Of the remaining objects, 100 sources are RRab's observed in the overlap regions between fields. These sources provide a useful test of the photometric calibration between CSS fields and

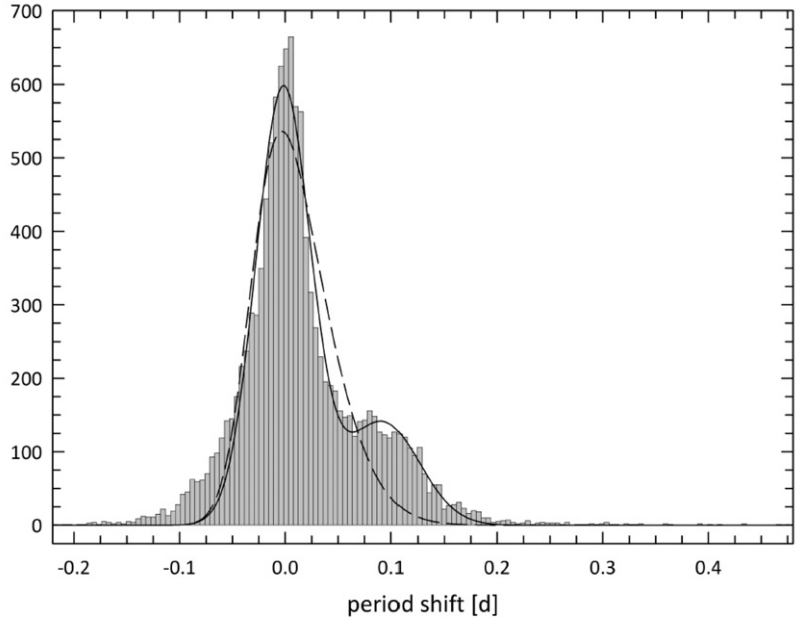

Figure 6. Period-shift distributions for the CSS RRab's. Here we plot the difference between the observed period and OoI period–amplitude line along with a two-Gaussian fit and a skew-normal fit to the resulting data.

Table 1
Parameters of RRab Stars

ID	R.A. (°)	Decl. (J2000) (°)	(V_0)	P (days)	A (mag)	N	d_h (kpc)	A_V	η	ID_{alt}
CSS_J000004.0+182425	0.01669	18.40698	15.17	0.4851599	0.97	201	7.86	0.055	53709.61433	...
CSS_J000009.3+053523	0.03901	5.58986	16.09	0.5760276	0.71	144	11.88	0.088	53730.28997	...
CSS_J000010.3−215515	0.04331	−21.92086	17.56	0.5047586	1.01	80	23.76	0.039	53673.54441	...
CSS_J000018.2−170421	0.07590	−17.07252	16.97	0.5182854	1.11	112	17.98	0.042	53705.36054	...
CSS_J000018.2+193253	0.07619	19.54824	15.66	0.5455067	0.85	211	9.73	0.088	53709.15681	V0420 Peg
CSS_J000032.1+225937	0.13380	22.99388	14.67	0.5906413	0.41	205	6.08	0.136	53709.52022	...
CSS_J000040.1+094718	0.16718	9.78848	16.76	0.6567631	0.55	222	15.16	0.235	53706.72679	...
CSS_J000047.9+185328	0.19997	18.89122	17.87	0.5065207	0.96	212	27.12	0.060	53709.45916	...
CSS_J000049.5+061402	0.20659	6.23398	16.94	0.4957843	1.11	197	17.35	0.097	53706.68568	...
CSS_J000051.6−170038	0.21520	−17.01077	16.16	0.6041318	0.61	112	12.51	0.046	53705.48548	...
CSS_J000108.2+130814	0.28455	13.13737	17.74	0.5902815	0.75	204	24.54	0.154	53709.70626	...
CSS_J000114.8−180617	0.31187	−18.10495	17.62	0.5818541	0.78	112	24.50	0.042	53705.58907	...
CSS_J000122.8−194327	0.34503	−19.72418	17.54	0.5402745	0.79	107	23.63	0.040	53705.16680	...
CSS_J000123.1−172950	0.34661	−17.49736	16.09	0.5353362	0.96	112	12.05	0.046	53705.36891	...
CSS_J000158.0+124240	0.49167	12.71114	14.74	0.6263317	0.55	206	6.20	0.156	53709.36654	Loneos-RR 770

Notes. Column 1: gives the CSS ID; Columns 2 and 3: give the right ascension and declination; Column 4: gives average magnitude from the Fourier fit to the light curve; Column 5: gives the period of the RRab; Column 6: gives the fit amplitude of variation; Column 7: gives the number of photometric observations; Column 8: gives the heliocentric distance to the RRab; Column 9: gives the extinction based on the Schlegel et al. (1998) reddening map; Column 10: gives the ephemeris of the RRab; Column 11: gives the IDs for sources that were previously known.

(This table is available in its entirety in a machine-readable form in the online journal. A portion is shown here for guidance regarding its form and content.)

the period determinations. In Figure 10, we plot the difference between the average fit magnitudes and periods of the RRab's overlapping between fields. This suggests that uncertainties in the photometric calibration between fields are generally <0.1 mag in agreement with the comparison with Landolt stars. We note that since overlapping objects are located on the edges of the fields, where the photometry is poorest, on average the photometry should be slightly better. In addition, we can see that the period determinations are in excellent agreement even though the total number of observations, and observation dates, vary between adjacent fields. For an RRab with a 0.6 day period, a 0.004% uncertainty corresponds to an uncertainty of only 2 s. Of the 100 objects, none differed by more than 0.007% in period, or more than 0.12 mag in V.

5. COMPARISON WITH RR LYRAE FROM PAST SURVEYS

To compare the CSS RRab parameters with those of known RRab's, we downloaded all the objects marked as variable sources in the Simbad database. This consisted of 41,765 objects. We also downloaded the International Variable Star Index (VSX, 2011 January edition; Watson et al. 2006) data set and extracted all the sources marked as RRL. This consisted of 24,124 objects. A small number of the VSX objects are duplicates based on their positions. Simbad and VSX data significantly overlap, yet both contain some unique sources. In the bulk of cases where the two sets match, the VSX data set is superior since it provides the periods for the RRLs.

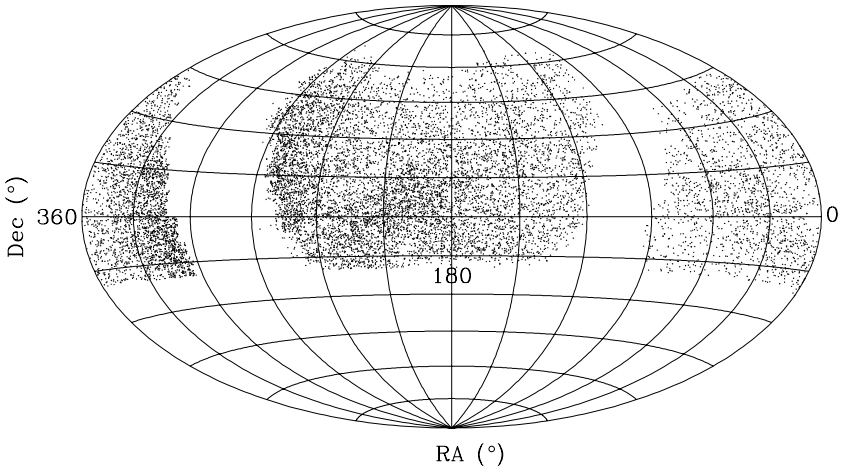

Figure 7. Aitoff projection of the equatorial coordinates for all the CSS RRab's detected in this work.

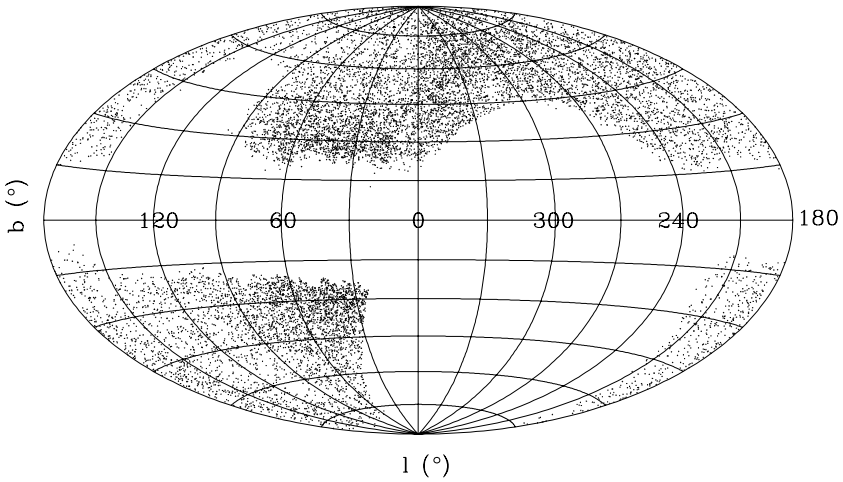

Figure 8. Aitoff plot of the Galactic coordinates of all the CSS RRab's detected in this work. The Galactic plane region with $|l| \lesssim 15^{\circ}$ is avoided by CSS because of source crowding.

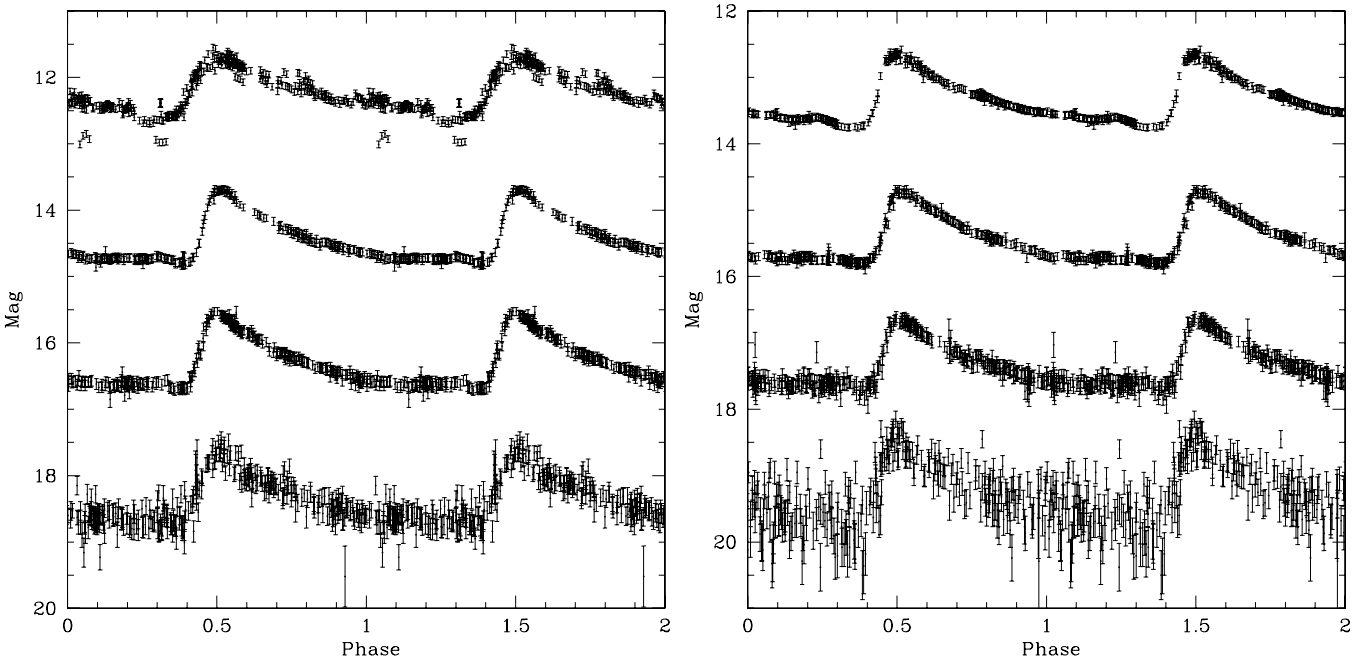

Figure 9. Examples of CSS RRL light curves phase folded with their best-fit periods. In the left panel, we plot the light curves of RRab's with average magnitudes of $V \sim 12.5$, 14.5, 16.5, and 18.5. In the right panel, we plot RRab's with magnitudes of $V \sim 13.5$, 15.5, 17.5, and 19.5.

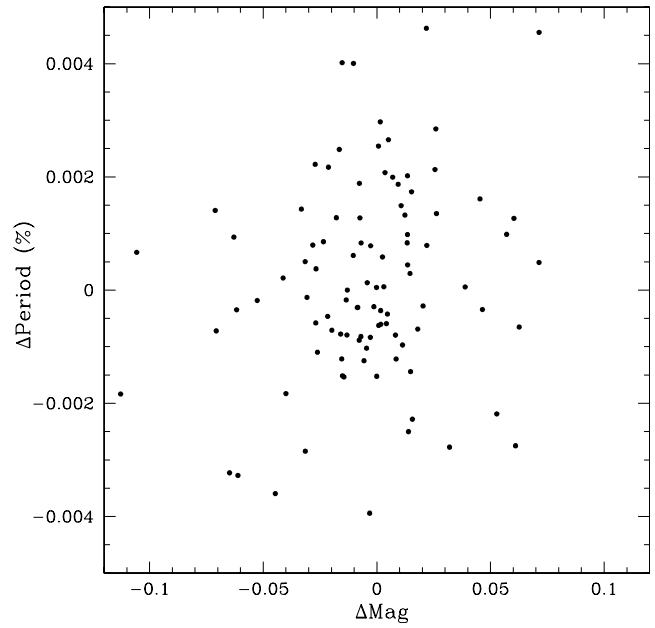

Figure 10. Distribution of the differences in the period and average magnitude *V* for 100 CSS RRab's that were detected in overlapping CSS fields.

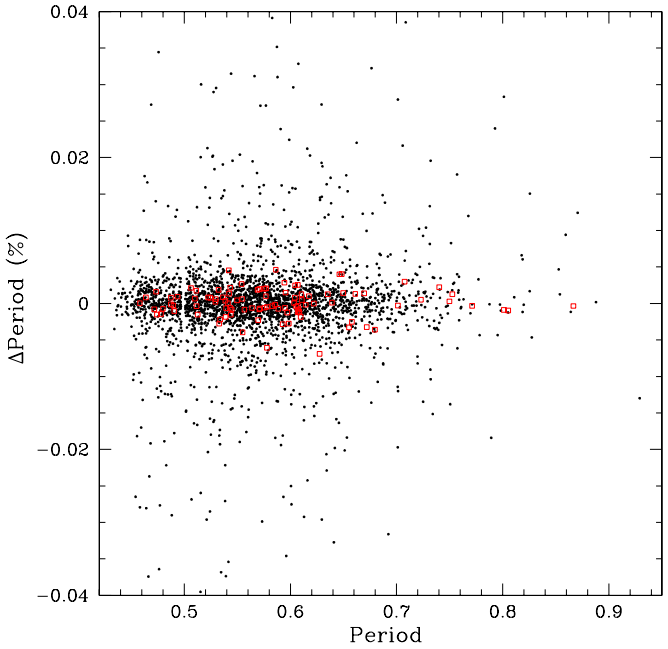

Figure 11. Uncertainties in CSS RRab period determinations. The black points show the percentage period difference between VSX and CSS periods for previously known RRab's. The boxes show the period differences for RRab with periods determined separately in two overlapping CSS fields.

(A color version of this figure is available in the online journal.)

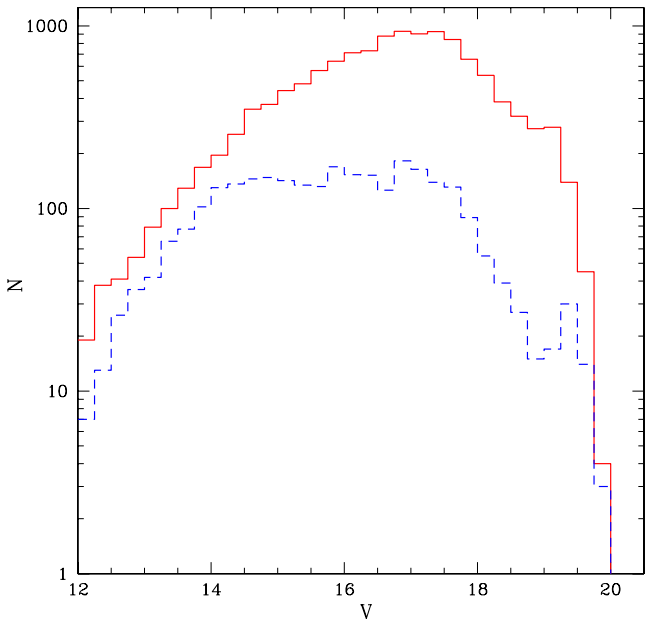

Figure 12. Magnitude distribution of CSS RRab's. The solid line shows a histogram of the average *V* magnitudes for RRab's discovered in CSS data. The dashed line shows the distribution of previously known RRab's recovered in this work.

(A color version of this figure is available in the online journal.)

We matched the RRab with the VSX and Simbad data sets and found 2136 matches to known Simbad variable sources and 2753 matches to VSX sources. In order to account for significant astrometric uncertainties in some of the older sources we used a large 10 arcsec matching radius. From the combined data sets we find matches to 2842 known sources. This is a small fraction of the total number of known RRLs. Most have been found by microlensing surveys that have almost exclusively covered the Galactic bulge and the Magellanic Clouds (e.g., Soszyński et al. 2009; Pietrukowicz et al. 2012). Additional large numbers of sources come from globular clusters near the Galactic plane that are not covered by CSS. Of the VSX RRab matches, 2727 objects have recorded periods. In Figure 12, we plot the magnitude distribution of the CSS RRLs compared to that of these previously known sources.

In Figure 11, we plot the percentage difference between VSX periods and those derived from CSS data for the matching previously known RRLs. As with the 100 overlapping CSS RRab's the scatter in periods is generally $\sigma \sim 0.002\%$. However, 397 of the RRLs have period differences of $>0.01\%$. Objects with this level of uncertainty would have a phase error of 0.1 over 1000 cycles (or time spans from one to three years for RRab). In 49 cases, the difference in period was greater than 1%. We checked the phased light curves for the 397 objects and found only two objects where the CSS period was incorrect. Four objects had similar light curve reduced χ^2 with both CSS and VSX periods. However, three of these were apparent aliases, since they were noted with periods <0.41 days. The remaining RRab's had a 0.012% period difference with both periods being equally likely. Of the objects with apparently incorrect VSX periods, 89 were from the NSVS sample (Kinemuchi et al. 2006) and 61 were from the LONEOS-I sample (Miceli et al. 2008). Since only 2 of the 2675 matching sources had clearly incorrect CSS periods we have high confidence in the periods derived here.

Figure 12 shows that most of the VSX–CSS matching sources are on average brighter than RRab in the full sample. This suggests that the matched objects will, on average, be better sampled and have a higher signal-to-noise ratio than the sources in general. It is likely that the faint CSS RRab's have less accurate periods than the bright ones.

In order to get an idea of our detection completeness we extracted light curves for all the VSX sources marked as possible RRab's within our survey region limits. We found CSS matches for 4144 VSX RRab sources. In a number of cases there were multiple VSX objects at the same location to within a few arcseconds. These sources are very likely duplicates.

Of the 1328 unique VSX RRab's with periods that were missed in our RRab selection process, 298 objects were not selected by our Welch–Stetson variability of $I_{WS} > 0.6$. Of these, 97 had either $V < 12.5$, and were either saturated, or had $V > 19$ and were too faint for us to detect their variability. Most of the remaining VSX objects not in among our candidate variables were poorly sampled. Many had fewer than the 40 measurements required for initial selection. Inspection of ∼100 of the CSS light curves for these sources showed that a dozen were not variable, and a couple of dozen were blended with nearby stars.

Of the remaining 1030 VSX sources selected as variable in CSS data, 627 had LS periods with significance below our threshold (that is, $p_0 > 10^{-7}$). Of these low periodic significance sources, 290 had periods outside our 0.36 day $< P <$ 1.4 day pre-selection window and 27 have VSX periods less than 0.4 days.

Inspection of the CSS photometry for the 403 remaining VSX sources with periods and significance within our selection range showed that 52 were not RRab, but RRc's and other types of variables. An additional 52 of the 403 sources are Blazkho RRLs (Blazhko 1907). These Blazhko RRab candidates were likely missed due to poor Fourier fits in the presence of phase variations. Among the remaining 299 candidates, 66 were poorly sampled and 233 had noisy CSS light curves due to blending and saturation effects.

Overall we find that ∼30% of the genuine RRab's in the VSX data set were missed in our selection because of their brightness (2%), blending (1%), poor or noisy light curve sampling (8%), period variations (1%), or inaccurate LS periods (17%).

5.1. Completeness

In order to better understand the detection completeness of our RRab sample we decided to simulate the detection of CSS RRab's from light curves through variability selection and processing with AFD software. This estimation process requires understanding the different sampling effects and variation in uncertainties between fields, as well as reproduction of realistic RRab light curves and underlying period distribution.

The CSS data set analyzed here contains 2454 separate fields. As shown in Figure 1, there is a significant range in the number of observations per field. The distribution of observation density on the sky is given on the Catalina data release Web site.[9] In our simulations we selected ∼5% (134) of the fields. The least sampled among these test fields had 35 observations while most sampled had 256. For each of the 134 test fields we measured the average magnitude and scatter in brightness for each source. We also determined the detection completeness as a function of magnitude for each image based on comparison with deeper co-added images. As systematic uncertainties are likely to vary between fields, we used the average source magnitudes and uncertainties to determine the scatter as a function of magnitude for each field. Since ∼5% of the photometry was found to contain outliers, we model the error distribution using two separate Gaussians with varying standard deviations. One reflects the 95% of good data and the remaining points model outliers.

To simulate realistic light curves, we selected 1010 high signal-to-noise CSS RRab's with average magnitudes $V < 16.5$, Fourier-fit reduced $\chi^2 < 1.5$, and more than 100 observations. The fits to these sources serve as templates. As the detection completeness depends on RRL period, it is necessary to select an underlying period distribution. Cseresnjes (2001) provides a sample of 3700 RRLs from a mixture of Sagittarius dwarf and Milky Way sources. We used this distribution to select periods for our test sources. The number of test sources in each field was chosen to exponentially increase with decreasing brightness so that many faint sources would properly sample the detection sensitivity for faint sources. Once a period is selected we find the closest match among the 1010 templates and combine this with the uncertainties observed for each field and brightness. We generated ∼100,000 artificial RRab light curves for sources with magnitudes from $V = 12.5$ to 20.5.

The artificial RRab light curves were all run through the same variability and period selection process as the real data. Of the 100,000 simulated objects, 15,271 were detected as variable sources and thus had their LS periods determined. Of these sources 11,543 were found to have periods within the range selected for RRab's and among these 10,483 (90%) were ultimately selected as RRab's via the AFD software.

In Figure 13, we show the distribution of recovered artificial RRab's. The error bars show Poisson uncertainties based on the number of detected sources. The figure suggests that real RRab's will be missed at all brightness levels. This result is in agreement with our comparison to VSX data. Also, few of the brightest sources are recovered because saturation effects cause large uncertainties. This figure combines the poorly sampled fields with well-sampled fields. On average the artificial light curves have fewer observations than the observed distribution and thus underestimate the average number of recovered sources. However, the plot clearly shows that many of the faint objects that are selected as variable sources are ultimately not recovered as RRab's. This result suggests that applying additional period finding searches on the millions of candidate variables may well lead to additional RRab discoveries. In particular, as the largest difference in recovery is at faint magnitudes, many distant RRab's may be recovered. However, period recovery at such low signal-to-noise may be difficult.

To investigate the dependence of completeness on the number of observations in a field, we combined the 134 fields into four groups: fields observed less than 100 times, fields observed between 100 and 130 times, fields observed 130–180 times, and fields observed more than 180 times. The completeness results for these groups are also shown in Figure 13. The figure clearly demonstrates the significant effect that increasing numbers of observations have. Much of the reason for this difference is mainly the decrease in photometric sensitivity with magnitude. For example, a 19th magnitude source is detected in less than half of the observations of a field. Thus, the number of points within the artificial light curves of faint sources is far fewer than the total number of observations. The average number of observations per field best matches the top curve we present, suggesting that ∼70% of the bright RRab's are recovered (in good agreement with the analysis above). We note that our completeness for small numbers of observations is in marked contrast to the results of Miceli et al. (2008) based on between 28 and 50 epochs of LONEOS data. However, these authors detected RRLs using a template fitting method. This is likely to be much more sensitive with a smaller numbers of observations and may also improve the recovery of faint RRab's.

6. ADDITIONAL INFORMATION FROM SDSS

For most CSS RRab's above declination ∼−2°, it is possible to check the accuracy of the transformed CSS photometry

[9] http://catalinadata.org

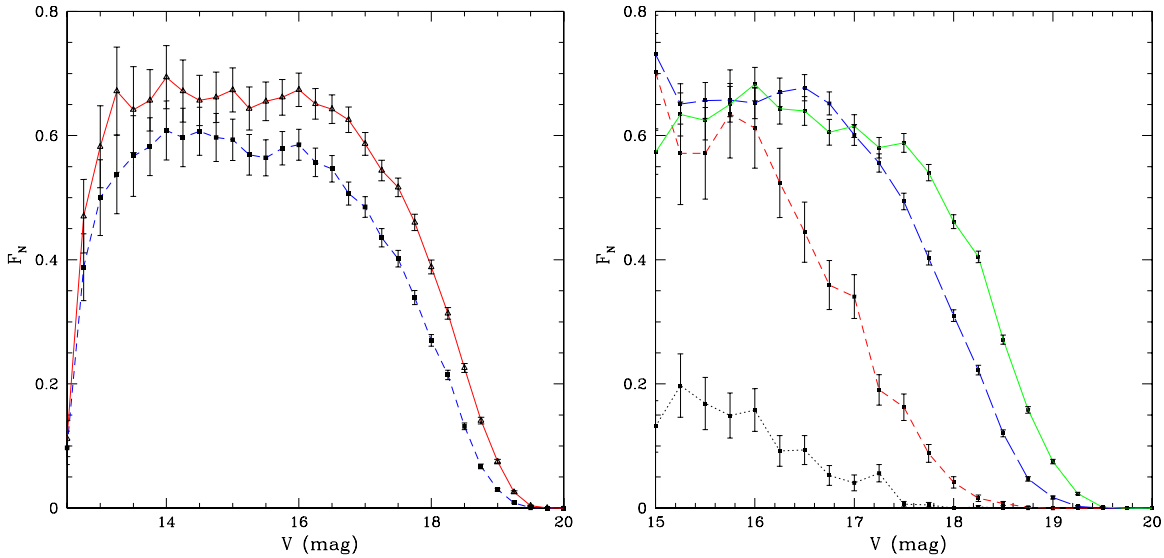

Figure 13. Detection completeness as a function of magnitude. In the left panel, we show the fraction of all artificial light curves that were selected as variables as the solid line. The dashed line shows the fraction after selecting an object in the correct period range and processing through the AFD software. In the right panel, we show the detection sensitivity for varying numbers of observations in a field. The dotted line shows the result for fields sampled an average of 80 times, the short-dashed line for fields sampled 115 times, the long-dashed line 160 times, and the solid line 200 times.

(A color version of this figure is available in the online journal.)

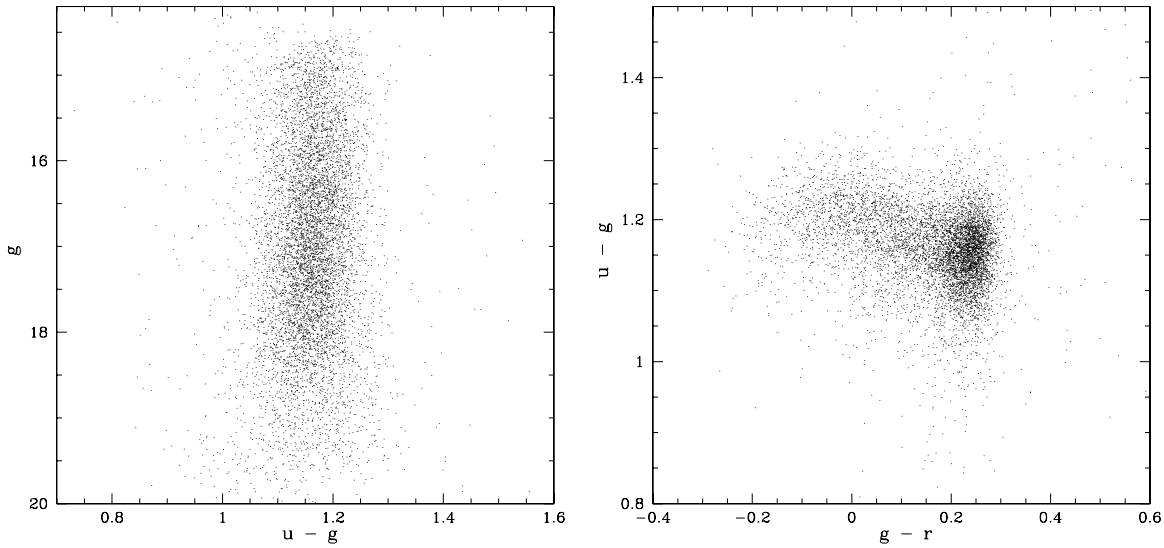

Figure 14. Extinction-corrected SDSS photometry for CSS RRab. Left: the color–magnitude distribution of the RRL. Right: the $g - r$ vs. $u - g$ distribution of the RRL.

using SDSS data. Within the stripe-82 region, the SDSS data have recently been shown to have photometric uncertainties of 1% or less (Ivezic et al. 2007). The SDSS data also reach objects significantly deeper than our RRL sample and provide spectroscopic information for very large numbers of sources in our RRab catalog.

6.1. SDSS Photometry

To carry out a photometric comparison we matched the locations of our RRLs using the SDSS cross-match service and a 3″ radius. We select the nearest source within this region as the best match. Of the 12,331 RRLs, we find 8746 sources in SDSS DR8 that match our RRab's. SDSS data saturate in r, i, and z for stars brighter than ∼14.5 and in u band at magnitude 16 (Chonis & Gaskell 2007). After removing the matching objects above the saturation limit we find 7788 sources with SDSS photometry. We correct for the extinction of SDSS photometry using the Schlegel et al. (1998) reddening maps and coefficients. In Figure 14, we plot the extinction-corrected g versus $(u - g)$ and $(u - g)$ versus $(g - r)$ photometry for the RRab's, and in Figure 15, we plot the $(g - r)$ versus $(r - i)$ and $(r - i)$ versus $(i - z)$ colors of the objects with SDSS photometry. The bulk of the sources are strongly clustered near $(g - r) = 0.25$ and $(r - i) = 0.1$ with a scatter of ∼0.1 mag. This suggests that the uncertainty in our absolute V magnitudes based on assuming the average $B - V$ of RRL is generally <0.05 mag.

Almost all of the RRab's lie within the SDSS color region selected by Ivezic et al. (2005). We inspected a number of the outliers and it was clear that a small number of the RRab's were blended with other stars, or galaxies, when compared to higher-resolution SDSS images. The flux from the additional source distorts the color of the object, increases the brightness, and typically reduces the observed amplitude of the variability.

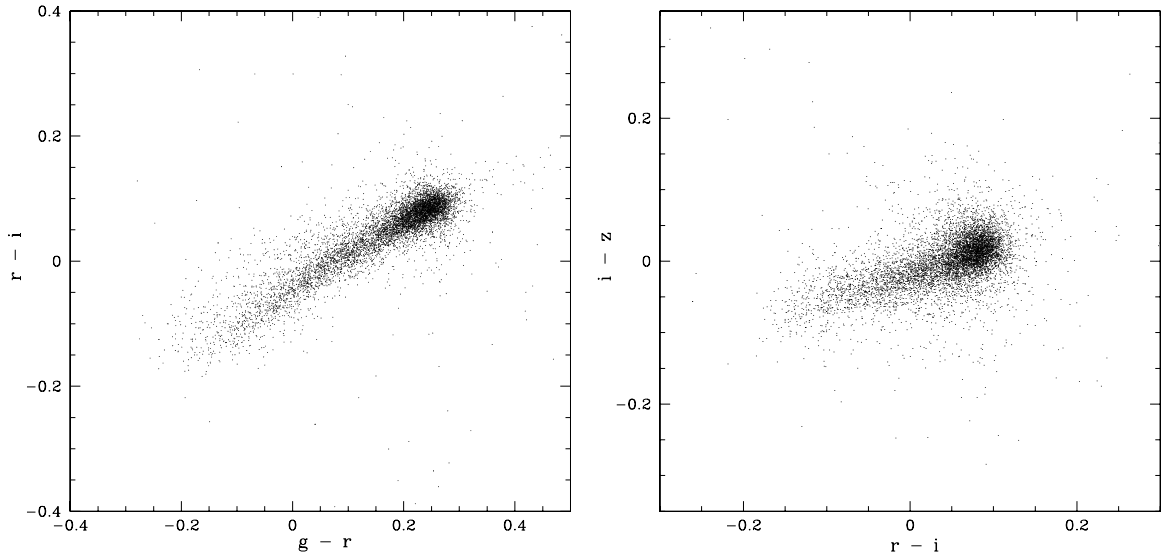

Figure 15. Extinction-corrected color–color plots for all CSS RRab with SDSS DR8 photometry. Left: SDSS $g - r$ vs. $r - i$ distribution of the RRL. Right: SDSS $r - i$ vs. i–z distribution of the RRL.

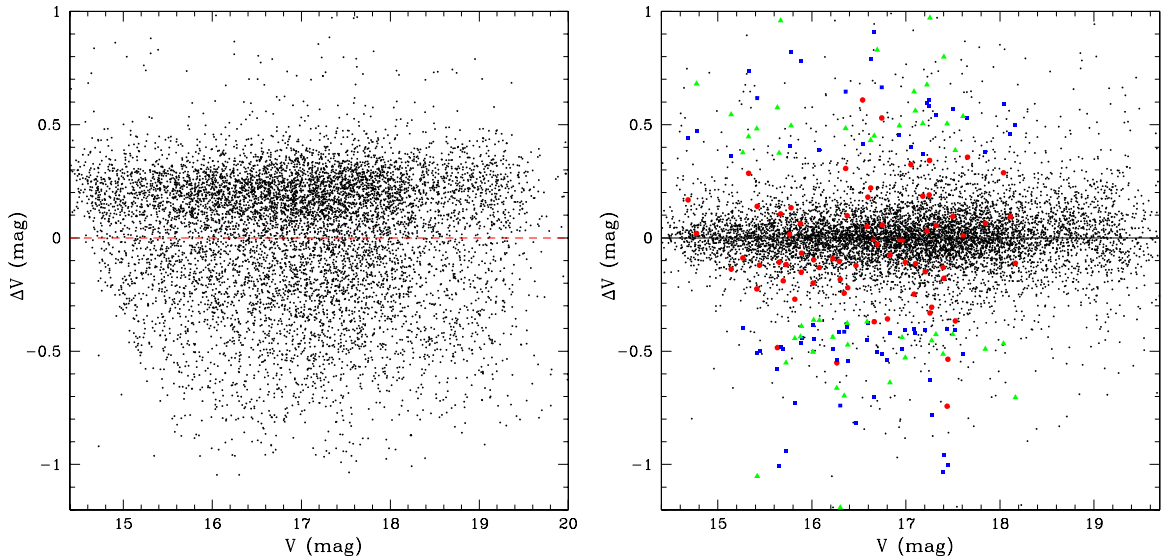

Figure 16. Difference between CSS and SDSS transformed magnitudes. Left: the difference between SDSS and CSS magnitudes transformed to V compared to those without correction for the observation phase. Right: the distribution of V-mag differences after correcting for SDSS observation phase. The green points show likely period changing RRab. The blue points show differences for bright outlier sources before periods were refined. The red points show the difference for the same sources with improved periods.

(A color version of this figure is available in the online journal.)

To compare the SDSS magnitudes to those derived from our calibration with Landolt standards, we first use the photometric transformations of Ivezic et al. (2007), which are themselves tied to Landolt standards via a large sample of Stetson (2000, 2005) secondary standard stars. Then following Sesar et al. (2010, their Equation (13)), we transform the extinction-corrected SDSS photometry to V magnitudes. This is a slightly different transformation than used with the BHB sample, since Ivezic et al. (2007) note that their calibration is not appropriate for BHB star colors.

In Figure 16, we plot the transformed values in comparison with the average CSS V magnitudes from the Fourier fits. The high degree of scatter ($\sigma = 0.28$ mag) is due to the observations being taken at random phases. Accurate observation times were calculated for each SDSS measurement. For each object we took the average observation time of the g and r measurements. The difference between these is only ∼4 minutes and thus very small in comparison to the RRab's periods. Using our Fourier fits we determine the phase of the RRab in the V-band light curves at the time SDSS observed it, and then we use the fits to calculate the V-magnitude offset at this phase. In Figure 16, we plot the magnitudes corrected for the SDSS phase offset. The overall reduction in scatter is evident. After 3σ clipping the clear outliers, the 1σ in magnitude difference is less than 0.12 mag and the average offset is 0.003 mag. This dispersion is much larger than for the BHB sample.

Like the BHB sample, the dispersion in the phase-corrected and transformed SDSS magnitudes includes errors in the SDSS photometry and uncertainties in the transformation from SDSS g and r to V magnitudes. However, additional scatter beyond the BHB sample is due to the uncertainties in the RRL periods (of order 0.002%) and the resulting phase corrections, since many

of the SDSS observations of these objects were made around 2001, while CSS observations were generally taken from 2005. For example, a 0.5 day period RRab undergoes ∼3000 cycles in four years. Over this period a 0.002% error in the period compounds to a phase offset of 0.06 (∼43 minutes). In RRab light curves, an error of ∼0.1 in the phase before the peak can correspond to a 1 mag variation in brightness. Taking this into account, the average magnitudes derived from the CSS light curves should have accuracy similar to the BHB sample, with some additional small uncertainty of up to 0.07 mag due to the assumption of an average RRL color (see Section 3).

To further investigate the source of differences in brightness we selected the 457 outlier RRab's with offsets >0.36 mag (3σ). From visual inspection, it was clear that approximately 50 exhibited period variations. The offsets due to period changes within these stars cannot be corrected without contemporaneous data. Such period changes are known to be common as Alcock et al. (2000, 2003) found 10% of the 6391 LMC RRab stars they observed to exhibit period changes. Many of the objects with offsets <0.36 mag will also exhibit period variations, thus increasing the observed scatter. A small fraction of the outliers were found to be due to sources that were blended in CSS images, yet were resolved in the SDSS data. Additionally, a small number of the objects were either matched to the wrong SDSS source or the SDSS photometry was clearly spurious. Of the remaining outliers, 68 had offsets due to slight errors in the period.

We interactively derived more accurate periods for 105 of the objects (including some likely Blazkho RRLs). The average difference between the original period and the new values was 0.0023%. In Figure 16, we also plot offsets for the original and improved periods for the 68 RRab's, as well as the offsets for period changing RRLs. Of the objects for which we obtained improved periods, eight remained with offsets >0.36 mag, yet we estimate that the errors in their new periods are <0.001%. Investigation of these sources revealed that they all had multiple epochs of SDSS photometry. It is possible that the SDSS photometry in the database comes from the second epoch of images. Additionally, four of the outlying sources were found not to be RRab's, reducing the total number to 12,227.

6.2. SDSS Optical Spectra

The SDSS has released spectra of almost 1.6 million objects of which 460,000 are stellar objects (Abazajian et al. 2009). Among these spectra are those from the SEGUE subproject which specifically consisted of 240,000 stars with $14.0 < g < 20.3$ examined in order to study the structure of the Galaxy (Yanny et al. 2009). A second SEGUE survey covering an additional 120,000 stars is yet to be released. Each SDSS spectrum covers the 385–920 nm range and has resolution $R \sim 2000$ with target S/N $\sim$ 25. Matching our data set to SDSS DR8 spectra we found 1871 matches.

6.2.1. Metallicities

Among the 1871 SDSS spectra, 237 are multiple-observation RRab's having a total of 632 spectra. Some of these sources have four or more observations. These sources provide an excellent way of determining the level of variation in the SDSS spectra for RRab's. In particular, RRLs are well known to exhibit significant variation in radial velocity measurements because of pulsation (e.g., Liu 1991). For this reason, metallicities are traditionally measured from the difference in spectral type at minimum light measured from hydrogen lines compared to estimated from the

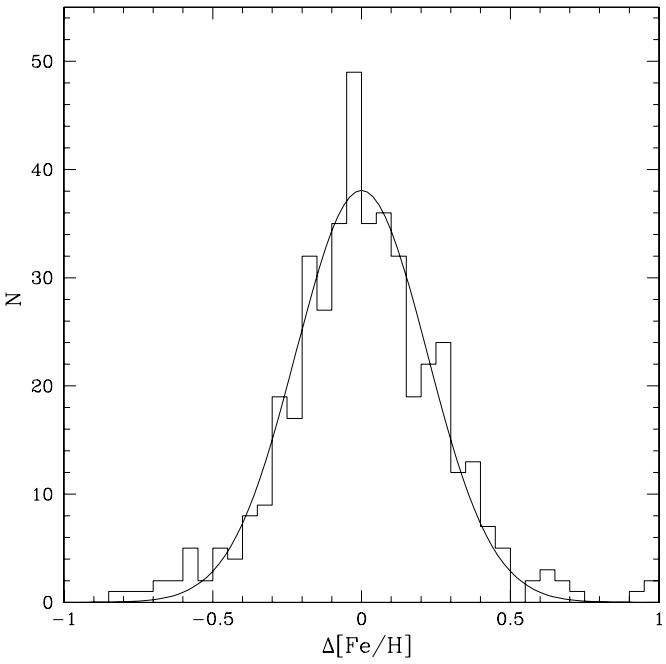

Figure 17. Distribution of differences in [Fe/H] calculated for RRab's with multiple SDSS observations. The curve shows a Gaussian fit to the data.

C II K line (Preston 1959). Butler (1975) extended this method so that values could be obtained at phases other than minimum light. Other methods of determining metallicity were also been devised using Ca II K equivalent widths (Clementi et al. 1991). Layden (1994, Figure 1) clearly shows the variation and overlap for hydrogen and calcium equivalent widths for RRLs of varying metallicities and derived an iterative method for determining metallicity.

In contrast to these methods, the SDSS team applied 12 separate methods for determining [Fe/H] in DR8 via the SEGUE pipeline (Lee et al. 2008, 2011). None of the methods used by SDSS exactly matches that applied to RRab's. The SDSS measurements are calibrated based on the known metallicities of globular clusters that were specifically covered for calibration purposes. The resulting values from the various methods are combined to provide an overall best value (FEHADOP) along with an uncertainty.

It is important to note that the spectra are taken irrespective of the phase of the sources. When the RRab's are far from minimum, light variations in the spectra are usually not used in metallicity determination, although For et al. (2011) suggest that spectra observed near maximum light can also be useful for abundance studies. SDSS spectra are also composites of multiple exposures. In most cases these consist of observations from three back-to-back 900 s exposures. However, the composites can be spread over days (Bickerton et al. 2012). This means that the RRab's have been observed at many phases.

To investigate the effect of phase variations in composite SDSS spectra on adopted metallicities, we calculated the variations in metallicity values for the objects observed on multiple nights. In Figure 17, we present a histogram of the single-object [Fe/H] variations. A Gaussian fit to the distribution gives $\sigma = 0.22$. The level of variation is consistent with the range of metallicities observed over a pulsation cycle by For et al. (2011). Thus, without considering any phase information the measurements are quite consistent. This simple match between repeated observations does not address possible systematic

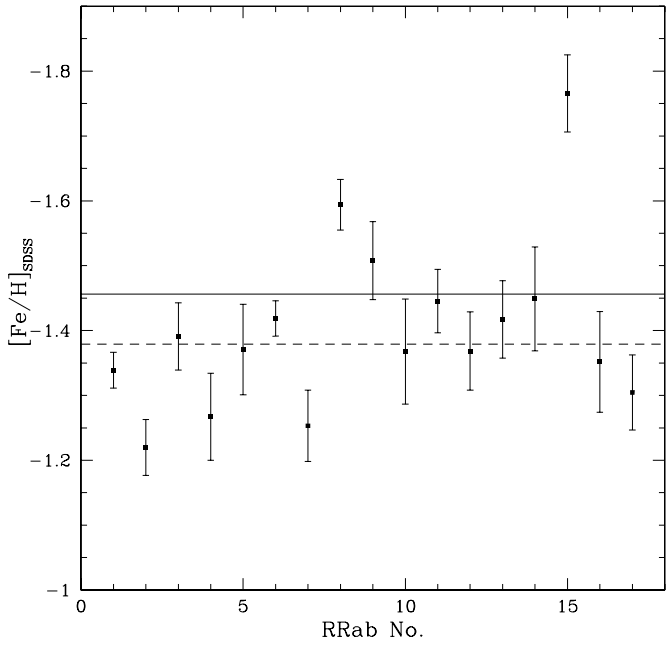

Figure 18. Distribution of metallicities for RRab's in NGC 5272 based on SDSS DR8 spectra. The solid line shows the average value while the dashed line shows the average from SDSS.

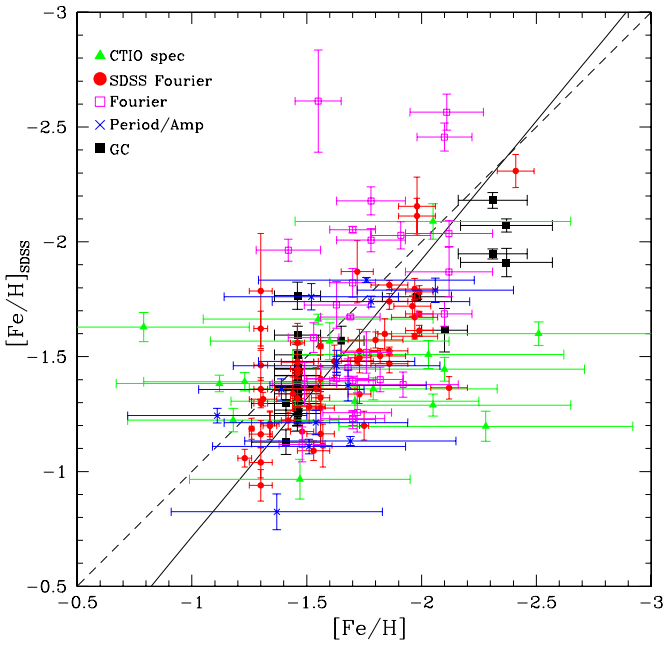

Figure 19. Comparison between RRab metallicities derived by De Lee (2008) and SDSS DR8 values. 26 additional globular cluster RRab's with SDSS spectra have been included. Each point is marked with a symbol presenting the method used to determine the value as noted in the text. A straight-line fit to the data is given by the solid line, whereas the dashed line shows the slope assuming no difference between the SDSS and De Lee (2008) values.

(A color version of this figure is available in the online journal.)

effects. To accomplish this we must undertake comparisons with known metallicities.

As globular clusters serve as metallicity standards, we searched for known RRab's within these associations. We matched the Samus et al. (2009) Catalog of Variable Stars in Globular Clusters (CVSGC) with spectra from SDSS DR8. We then removed the non-RRab variables based on previous classifications of the underlying sources as well light curves extracted from Catalina. Of the 52 variables with SDSS spectra, 26 were found to be RRab's, and among these 17 were from the well-studied cluster NGC 5272 (M3).

Numerous surveys have measured the metallicity of NGC 5272 (e.g., Zinn & West 1984; Armosky et al. 1994; Kraft et al. 1992; Sandstrom et al. 2001; Cohen & Melendez 2005; Cacciari et al. 2005). Based on the results from these surveys we find an average metallicity of [Fe/H] = −1.46. From the range of measurements we estimate the uncertainty to be ∼0.1. In Figure 18, we plot the metallicities and uncertainties for the RRab's provided by SDSS DR8. After removing a single outlier (the most distant RRab at 7.4 half-light radii with [Fe/H] = −1.76), we find average [Fe/H] = −1.38 ± 0.10. Cacciari et al. (2005) recently undertook an analysis of NGC 5272. Based on 45 RRab's they found [Fe/H] = −1.39 ± 0.11. The level of agreement in this case is clearly very good. However, NGC 5272 only serves as a single calibration point.

To investigate this further, we searched the literature to find metallicities for other RRab's. Although a moderately large number of RRab's have known metallicity (e.g., Layden 1994; Jurcsik & Kovacs 1996), almost all the stars surveyed are brighter than the SDSS $i = 15$ threshold for spectroscopic observations. However, De Lee (2008) provides [Fe/H] for more than 200 RRab's observed over a range of metallicities. This work comes from extensive analysis of SDSS and CTIO spectra as well as from photometry-based metallicities using the Fourier method of Jurcsik & Kovacs (1996) and period–amplitude method of Sandage (2004). Although De Lee (2008) undertook their own analysis of SDSS spectra, comparison of SDSS DR8 values to those derived from the same underlying data would likely contain a significant bias. Therefore, we restrict our comparison to the remaining 253 De Lee (2008) values. For these sources we find a total of 190 SDSS spectra with [Fe/H] values. Of these, 15 sources have metallicity based on CTIO spectra, 57 use the Fourier method on SDSS light curves, 26 are based on Fourier analysis of De Lee (2008) photometry, and 13 use the photometric analysis from the Sandage (2004) period–amplitude method. In Figure 19, we plot a comparison between the SDSS metallicities and those from De Lee (2008). In addition, we include the 26 globular cluster RRab's with SDSS metallicities. Linear regression of the data gives

$$[\mathrm{Fe/H}] = 0.828 \times [\mathrm{Fe/H}]_{\mathrm{SDSS}} - 0.408. \quad (4)$$

The overall result shows that the SDSS RRab metallicities are overall slightly higher than expected. After subtracting the linear fit from the data, the level of scatter matches that observed for repeated SDSS observations ($\sigma = 0.22$). This suggests that the SDSS values are characterized by this level of uncertainty. It may be possible to obtain more accurate values of metallicity using values derived from individual SDSS exposures as noted by De Lee (2008). In this way one could correct for the phase of the SDSS observations. An alternate method of determining metallicities for RRLs observed at random phases has been developed by For et al. (2011). Reanalysis of the spectra using this method may also yield improved results.

In Figure 20, we present the distribution of RRL metallicities derived from SDSS spectra corrected by Equation (4). The distribution itself peaks near [Fe/H] = −1.55 and exhibits a long tail extending to very low metallicities.

6.2.2. Radial Velocities

As we noted above, there is a well-known dependence of radial velocity on observational phase. The size of these

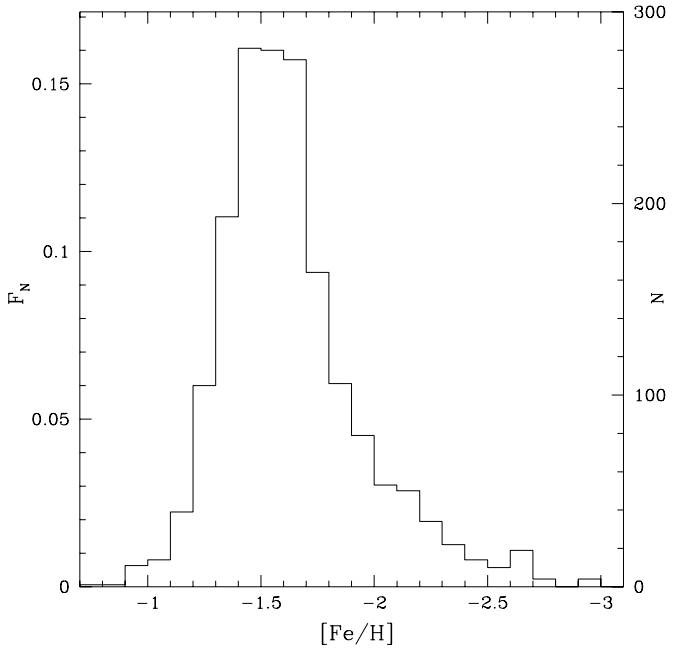

Figure 20. Metallicity distribution of 1382 RRab's in the CSS sample from 1749 SDSS spectra with metallicity measurements. Fractional numbers of RRab, F_N, are plotted on the ordinate axis.

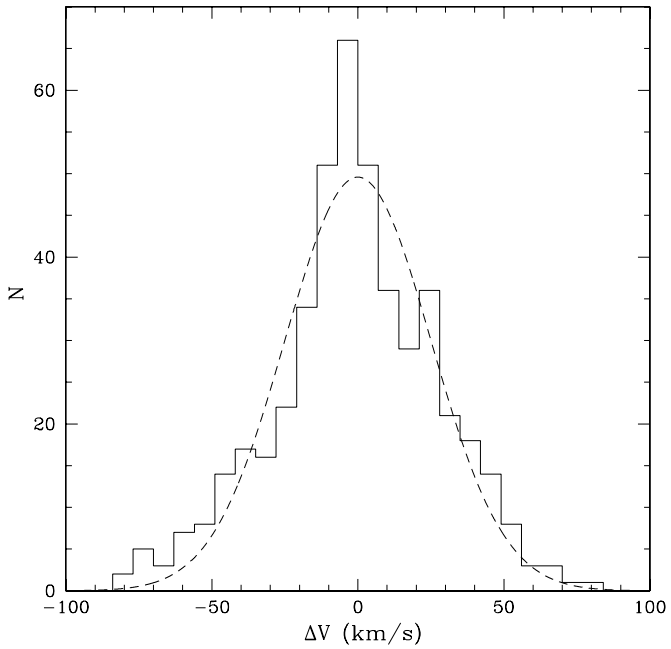

Figure 21. Distribution of differences in RRab radial velocities calculated from pairs of SDSS spectra. The dashed line presents a Gaussian fit to the distribution.

variations has been measured from repeated observations of RRLs (e.g., For et al. 2011). Apart from small uncertainties in heliocentric corrections, the difference between repeated observations of RRab's will reflect the pulsational variation. Therefore, following our metallicity analysis we determined differences in the velocity measurements between pairs of SDSS spectra. In Figure 21, we present a histogram of these velocity variations. Fitting a Gaussian to the distribution we find $\sigma = 25$ km s^{-1}. As expected, this dispersion is much greater than the uncertainties quoted by SDSS for the individual radial velocity measurements.

As SDSS observations are composites from multiple exposures, the pulsational signal from an RRab can be washed out if spectra are combined from varying phases. To determine radial velocities of the RRab's, we initially extracted the SDSS observation start and end times from the SDSS DR8 database. We then removed SDSS spectra where the difference between the start and end times of the observations was greater than 3 hr. This left a set of 1239 spectra of the original 1871. In most cases, the total time span of the remaining observations was around an hour.

Apart from problems of spectra being taken at indeterminate times, one must consider the importance of the phase at which the observations were taken. Sesar (2012) note that observations taken after phase 0.95 exhibit rapid velocity variations and therefore have uncertain velocity corrections. Using our Fourier fits to the RRab light curves, we derive the phase range over which the RRab spectra were taken. The average phase length of SDSS observations for the 1239 remaining RRab spectra was 0.087. Since there is uncertainty in the exact phases of the RRab's at time of the SDSS observations (due to uncertainties in their period), we decided to remove RRab's with SDSS observations that began before phase 0.1, or ended after phase 0.95. The final set consists of 905 spectra (less than half of the original set).

To accurately correct for velocity variation one must also consider how the radial velocities were measured. SDSS radial velocities are derived from both the metallic and hydrogen lines. Sesar (2012) recently noted differences between velocities measured using hydrogen and metallic lines as references and derived relationships for correcting these. These authors found that the combination of three Balmer lines would lead to uncertainties of a few km s^{-1}. We compared corrections based on combinations of Balmer as well as metallic lines and found typical differences of less than 10 km s^{-1}. We combined the relationships given by Sesar (2012) to produce an appropriate correction for the SDSS measurements. Using the Sesar (2012) velocity curves and amplitudes we then determined pulsation corrections for each of the 905 spectra by averaging the velocities over the period between the start and the end phase of the SDSS observations.

After correcting for pulsation velocities we redetermined the distribution of velocities for objects that had repeated observations. Because there are fewer spectra in the reduced set, the number of repeat observations is greatly diminished. In Figure 22, we plot the resulting distribution. A Gaussian fit to the distribution gives $\sigma = 14.3$ km s^{-1}. Clearly, the pulsational velocity corrections have improved the agreement between successive measurements of the radial velocities. We adopt this level of uncertainty for all the remaining spectra and do not consider the other spectra. We also recalculated variations in the metallicities for these 905 spectra and found no change in the standard deviation.

Analysis of radial velocities based on individual SDSS exposures has been performed by De Lee (2008) for RRab's found in stripe 82. Application of this technique can remove problems associated with composite SDSS spectra. Indeed, additional analysis of SDSS RRab spectra is underway by N. De Lee et al. (in preparation). This work should be able to recover radial velocities for the RRab's excluded here.

In order to understand the RRab radial velocities in the context of Galactic structure, we follow Law & Majewski (2010, hereafter LM10) and transform the velocities to the Galactic standard of rest (GSR). We assume a solar peculiar motion of $(U, V, W) = (9, 12 + 220, 7)$ km s^{-1} in the Galactic Cartesian

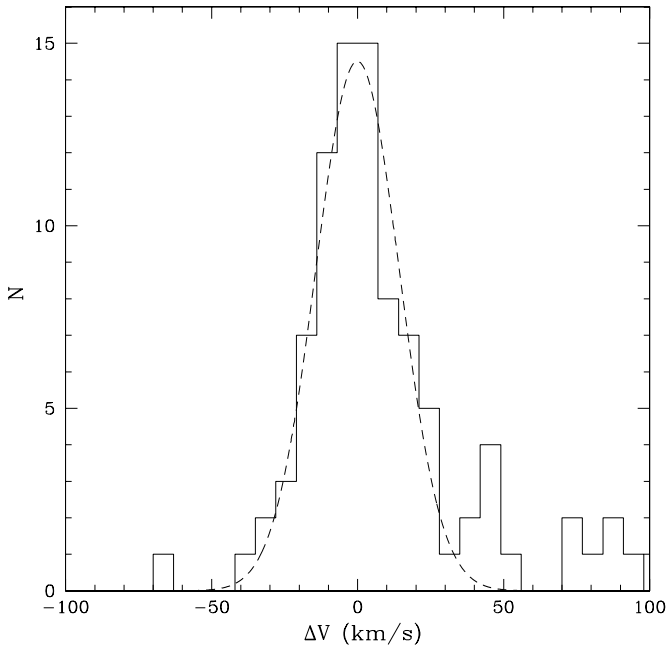

Figure 22. Distribution of differences in RRab radial velocities calculated from pairs of SDSS spectra after corrections have been made for pulsational velocity. The dashed line presents a Gaussian fit to the distribution.

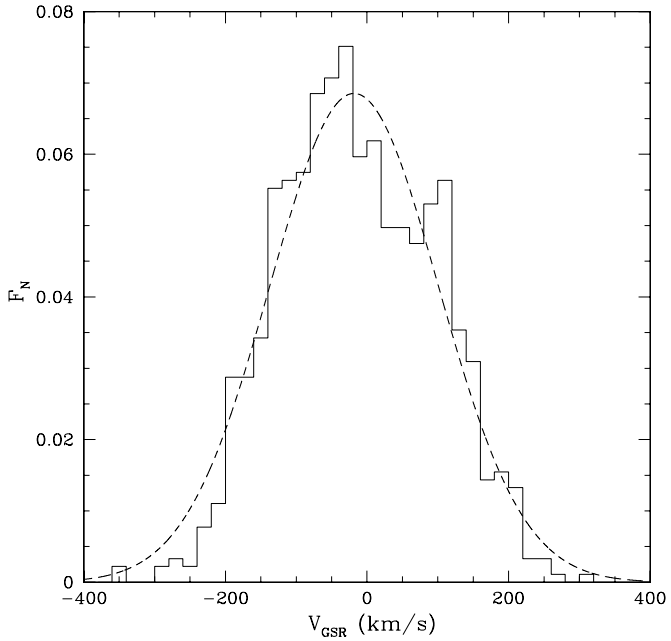

Figure 23. Distribution of RRab radial velocities relative to the Galactic standard of rest (V_{GSR}). This histogram contains values for the 905 CSS RRab's with SDSS DR8 radial velocity measurements. The Gaussian fit to the distribution is also plotted. The plot presents the fractional number of objects, F_N.

coordinate system. In Figure 23, we plot the distribution of velocities using a 20 km s^{-1} bin size. A Gaussian fit to the distribution gives mean $V_{GSR} = -18.3$ km s^{-1} and dispersion $\sigma = 119.0$ km s^{-1}. The distribution appears to show some non-Gaussian structure. However, there is likely some observational bias caused by preferentially detecting nearby sources.

7. RRab DISTANCES

The absolute magnitudes of RRab's are given by Catelan & Cortés (2008):

$$M_V = 0.23 \times [\mathrm{Fe/H}]_{ZW84} + 0.948, \quad (5)$$

where $[\mathrm{Fe/H}]_{ZW84}$ is the metallicity in the Zinn & West (1984) scale. The average metallicity for our RRLs with SDSS matches is [Fe/H] $= -1.48$. Thus, we adopt an average magnitude $M_V = 0.61$. This value is close to the value of 0.6 adopted by Keller et al. (2008) and Sesar et al. (2010). Like the SDSS photometry, the CSS V magnitudes were corrected for extinction using Schlegel et al. (1998) reddening maps. The dispersion in the metallicity is approximately 0.3 dex, which corresponds to a variation of 0.07 mag. The uncertainties in RRab absolute magnitudes are sometimes noted as ∼0.05 mag. However, the level of agreement between independent measurements (e.g., Benedict et al. 2011, their Table 10) suggests that true uncertainties are closer to ∼0.1 mag. The distances to individual sources are determined using

$$d = 10^{((V_0)_s - M_V + 5)/5}. \quad (6)$$

Here we have corrected the average RRab V_0 magnitudes to static values $(V_0)_s$ using values derived from a polynomial fit to the amplitude corrections given by Bono et al. (1995). Combining the uncertainties from the photometric calibration and color variation of 0.09 with the variations in metallicity and uncertainty in RRab absolute magnitudes, we derive an overall uncertainties of 0.15 mag. This corresponds to a ∼7% uncertainties in distances. From our photometric calibration, it is clear that faint RRL will have larger uncertainties in average magnitude. However, these uncertainties should generally not exceed 0.25 mag (∼12% in distance). The faintest CSS RRab's in our data set have $V \sim 19.5$, corresponding to 60 kpc. In Table 2, we present the u, g, r, i, z magnitudes, metallicities, and radial velocities transformed to the GSR for sources covered by SDSS DR8.

8. GALACTIC STRUCTURE

As the Sgr stream is near the ecliptic plane and our spatial coverage is complete in ecliptic longitude (λ) (apart from the Galactic plane region), in Figure 24 we plot the distribution of RRab distances and magnitudes versus λ. The Sgr streams are relatively clear in both plots. However, the magnitude plot gives a clearer picture of the inner (trailing) stream, showing two clear arms of the Sagittarius remnant at relatively small Galactocentric distances. One arm extends from $V \sim 19.25$ (54 kpc) at $\lambda = 225°$ to $V \sim 17$ (19 kpc) at $\lambda = 120°$. The other goes from $V \sim 18.5$ ($d = 38$ kpc) at $\lambda \sim 60°$ to $V \sim 17$ ($d = 19$ kpc) at $\lambda = 305°$.

Of the RRLs, 11,019 are at Galactocentric distances $d_G <$ 33.5 kpc and 1208 are beyond that. Since our detection completeness for the distant RRab's is much lower than the nearby brighter sample, it is clear that there are a significant number of RRLs within the Galactic halo.

In Figure 25, we plot the distribution of spectroscopic metallicities for the 219 RRab's with $d_G > 33.5$ kpc. Each value has been corrected via Equation (4). The distribution appears slightly more metal-poor than the overall distribution. The dispersion remains the same at around 0.3 dex and suggest that the objects are a mixture rather than a single population. A number of the sources have metallicity close to [Fe/H] $= -2.2$.

These halo RRab's have significantly lower metallicities than observed for M giants in the Sgr stream given by LM10 (⟨[Fe/H]⟩ ∼ −0.9). However, M giants and RRLs are known

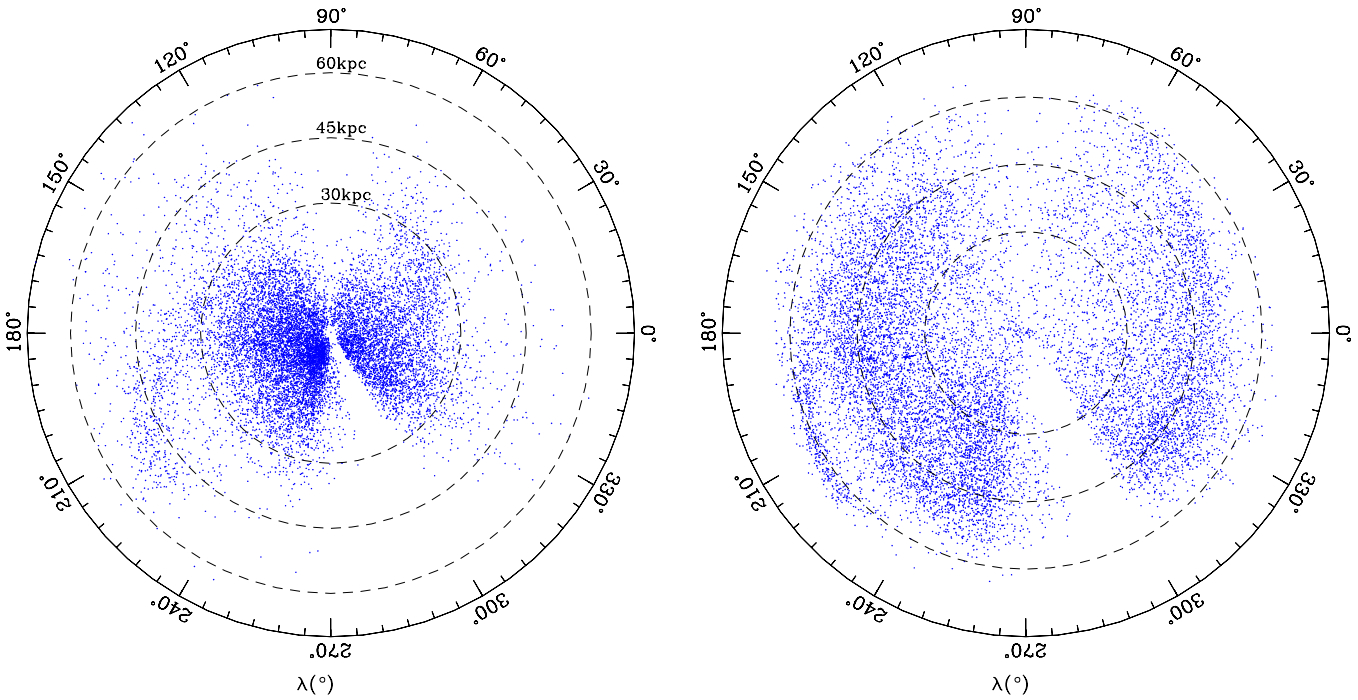

Figure 24. Magnitude and distributions of CSS RRab in ecliptic coordinates. The left plot gives the distribution of the RRab heliocentric distances. The right plot gives the distribution of magnitudes for RRab with $(V_0)_S > 14$. Here the dashed lines are set at magnitudes $V = 15$, 17, and 19.

(A color version of this figure is available in the online journal.)

Table 2
SDSS Data for CSS RRab Stars

ID	u_0	g_0	r_0	i_0	z_0	V_{gsr} (km s^{-1})	[Fe/H]
CSS_J004056.6−020802	18.19	17.03	16.76	16.69	16.63	...	...
CSS_J003621.0−015958	17.55	16.45	16.15	16.08	16.07	...	...
CSS_J004212.4−004251	18.22	17.16	16.91	16.82	16.81	123.7	−2.19
CSS_J004424.5−002743	18.97	17.88	17.59	17.51	17.49	−78.6	−1.47
CSS_J005150.9−024858	17.05	15.96	15.74	15.69	15.68	...	...
CSS_J005328.6−004321	19.03	17.84	17.59	17.57	17.55	−134.1	−1.71
CSS_J004923.6−001800	18.98	17.76	17.51	17.48	17.44	−89.5	−1.20
CSS_J005338.1−000303	17.76	16.73	16.44	16.42	16.38	...	−1.92
CSS_J010533.7−002344	19.30	18.20	17.96	17.91	17.88	...	−1.82
CSS_J011742.0−020819	17.11	16.02	15.82	15.74	15.75	...	...
CSS_J011723.6−020434	18.50	17.38	17.12	17.02	16.99	...	...
CSS_J011046.4−020214	18.71	17.61	17.41	17.41	17.35	...	...
CSS_J012924.9−024121	19.23	18.13	17.91	17.82	17.85	...	...
CSS_J012159.8−014415	19.21	18.07	17.80	17.71	17.71	...	...
CSS_J012206.6−011023	17.65	16.53	16.40	16.33	16.36	...	−2.32

Notes. Column 1: gives the CSS ID; Column 2–6: give the extinction-corrected SDSS magnitudes of the RRab; Column 7: gives the velocity in the galactic standard of rest, based on SDSS spectra; Column 8: gives the metallicity based on SDSS spectra.

(This table is available in its entirety in a machine-readable form in the online journal. A portion is shown here for guidance regarding its form and content.)

to trace different populations. Nevertheless, Casey et al. (2012) discovered a number of Sgr K giants with $\langle$[Fe/H]$\rangle \sim -1.7$. With the significant level of uncertainties the result is also consistent with Stripe 82 RRL in the Sgr stream measured by Watkins et al. (2009) with [Fe/H] $= -1.41 \pm 0.19$ and that of [Fe/H] $= -1.76 \pm 0.22$ measured by Vivas et al. (2005) for 12 Sgr stream RRLs.

8.1. Comparison with the LM10 Sagittarius Model

In order to compare our results further with models of the Sgr stream we first select the 905 RRab's with SDSS radial velocity uncertainties of $\sigma = 14.3$ km s^{-1}. We then find sources with Galactocentric distances >30 kpc and coordinates within range of the Sagittarius stream based on the Majewski et al. (2003) Sgr stream coordinates ($-15^\circ < B < -15^\circ$). For comparison, we select LM10 data points in this same region. In Figure 26, we compare the SDSS data with this LM10 model. The bulk of sources are a very good match to the model. However, compared to the model, the RRab's in the region $110^\circ < \alpha < 180^\circ$ appear to show a velocity trend with much larger velocities than the LM10. The region $250^\circ < \alpha < 360^\circ$ is not plotted since it is very poorly covered by SDSS data.

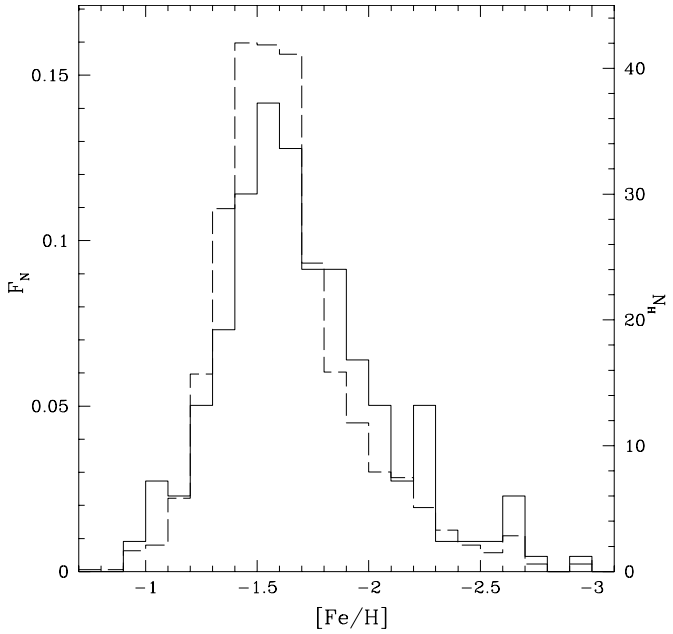

Figure 25. Distribution of SDSS metallicities for Galactic halo RRab's with Galactocentric distances $r_G > 33.5$ kpc. Here, F_N is the fractional number of RRab's and N_H the actual number of Halo RRAb's. The solid line gives the halo RRab's and the dashed line gives the distribution for all CSS RRab's with SDSS metallicities.

To compare the distant RRab distribution with the LM10 model we determine Galactocentric distances for all the objects. We next separate the RRab's into four groups, namely, a sample at distances $r_G < 33.5$ kpc and three more distant halo RRab samples with ranges 33.5–38 kpc, 38–45 kpc, and 45–65 kpc. These distance ranges were chosen to broadly separate the 1468 RRab's at distances >33.5 kpc into three similar groups of ∼500 RRLs each. In Figure 27, we plot the distribution of the Halo RRab's among the sample along with the LM10 model. The Sgr stream is clearly visible. However, many RRab's are seen in the region $110° < \alpha < 180°$ beyond 45 kpc and are not explained by the LM10 model. Additionally, many distant RRLs are found in locations not expected from the Sgr model. There is no obvious division of the Sgr RRab's into two streams as discovered by Belokurov et al. (2006) and Koposov et al. (2012).

To further investigate the Sgr stream, based on Figure 24, we select the clear Sgr RRab with $d_h > 30$ kpc in the region of $-41° < B < 31°$. We determined the density distribution and plot this in Figure 28. After binning the data in 2° bins we find that the main density distribution is well described by a single Gaussian centered at $B = -1.^\circ4 \pm 0.^\circ3$, with $\sigma = 6.^\circ8 \pm 0.^\circ3$, plus a background of 13.8 ± 1.6 for the RRab's. Here the number of Halo RRab's is a factor of ∼200 smaller than main-sequence turnoff (MSTO) stars analyzed by Koposov et al. (2012). Thus, although there is no obvious evidence for a second peak near $B = -8°$, we can conclude that the RRab's are distributed across the two streams (seen in SDSS MSTO stars and 2MASS M giants), rather than limited to one.

In Figure 29, we plot the distribution of heliocentric distances for the RRab's. The Sgr streams are clearly seen rising up to heliocentric distances of ∼52 kpc near $\alpha = 230°$ and 30 kpc near $\alpha = 70°$. We also include the M giant selected by LM10 as leading and trailing Sgr stream sources. The RRab's appear to have distances consistent with the M giants, although with significantly less scatter. We note that Newberg et al. (2003) found a 13% difference in the distance to the Sgr stream when comparing A-colored stars, such as RRL and BHB stars, to M giants, which is not confirmed in this study.

In Figure 29, we also compare the results with the Sgr stream *N*-body model of LM10. For an improved comparison, we apply extinction to each of the LM10 data points and remove sources that would have apparent magnitudes corresponding to RRab's beyond our detection limit ($d_h \sim 60$ kpc). We also remove points within 15° of the Galactic plane, since this region is not covered by CSS data. Although there is some overall agreement, at distances less than 20 kpc the presence of Galactic halo RRL is a significant factor, making comparison with the predicted nearby streams difficult. This is particularly the case near the Galactic center. We overplot two lines that clearly demonstrate the difference in distances between the LM10 *N*-body model

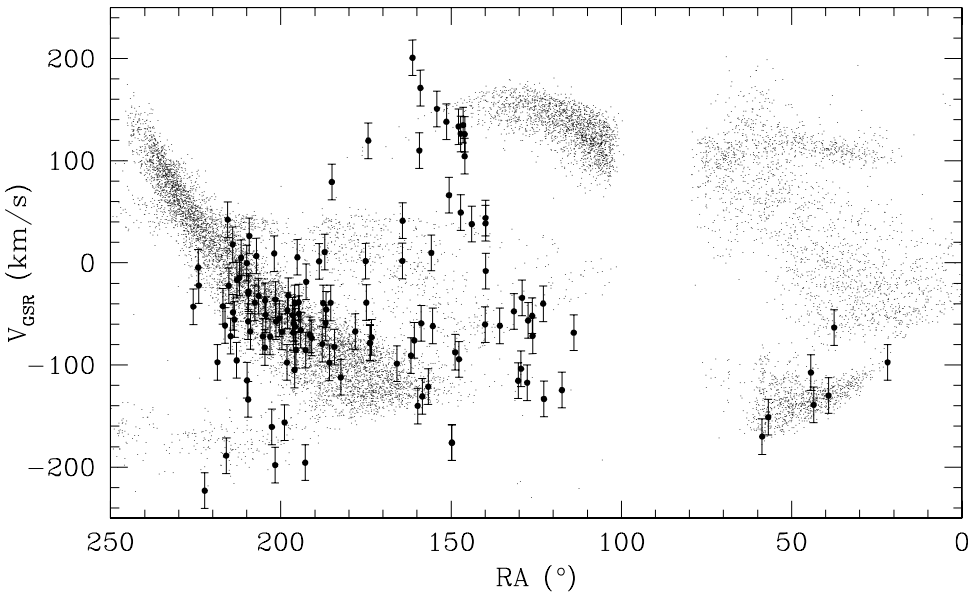

Figure 26. Distribution of Halo RRab radial velocities for possible Sgr stream members. The large dots show the SDSS radial velocities relative to the Galactic standard of rest for CSS RRab's with $d_h > 30$ kpc, and $-15° < B < -15°$ in Sgr stream coordinate system (Majewski et al. 2003). In addition, the velocities are plotted for LM10 model data points within the area and distance range covered by the CSS data.

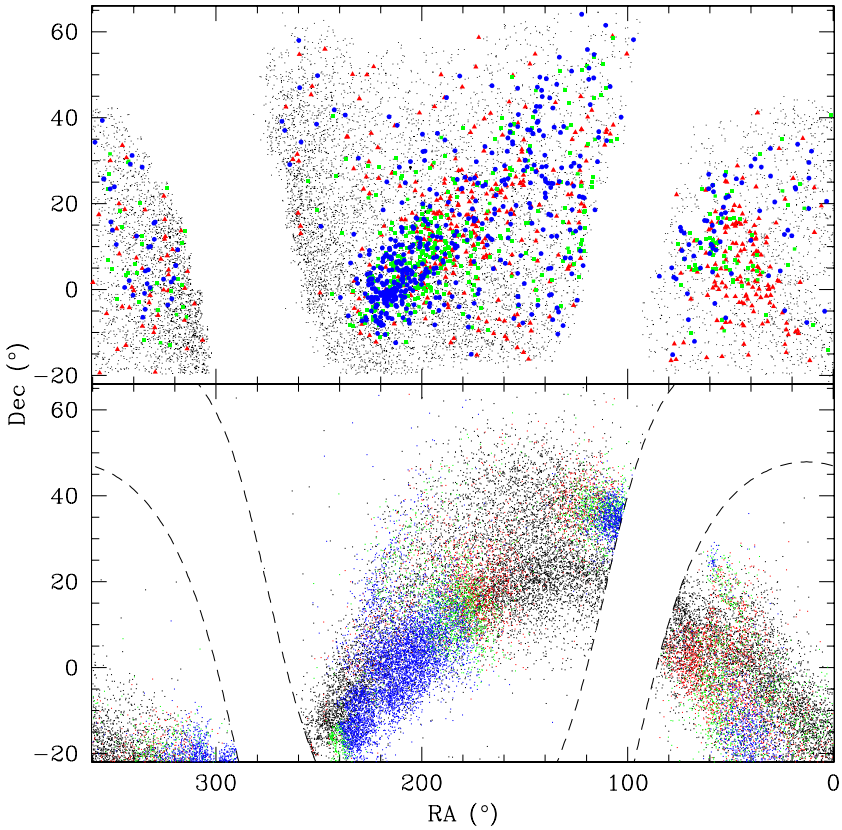

Figure 27. Spatial distribution of CSS RRab's. In the top panel we plot CSS RRab's at Galactocentric distances <33.5 kpc as black points, 33.5–38 kpc as red triangles, 38–44 kpc as green squares, and 44–65 kpc as blue circles. In the bottom panel we plot points from the LM10 model using the same colors.
(A color version of this figure is available in the online journal.)

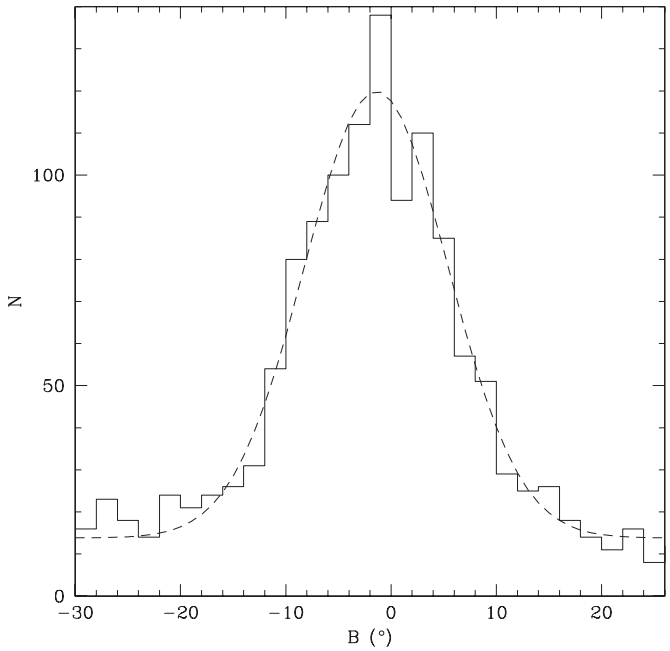

Figure 28. Density distribution of RRab's with $d_h > 30$ kpc in the Majewski et al. (2003) Sagittarius stream coordinate system. The dashed line presents a Gaussian fit to the data.

and the observational data. The model predicts stars ∼5 kpc farther than observed. This is expected since LM10 found that their model predicted fainter K_s magnitudes for M giants than observed.

Other differences include the Sagittarius leading arm near $d_h = 45$ kpc, $\alpha = 235°$. Although there appear to be stars near this location, the density is much lower than predicted by the LM10 model.

The distances of RRab's in the Sgr leading arm are found to vary by up to ∼10 kpc (corresponding to 0.37 mag). As 3σ uncertainties in the RRab magnitudes are ∼0.3 mag, the intrinsic depth of the leading Sgr stream is expected to be significantly less than 10 kpc.

Furthermore, there is only a weak sign for an Sgr leading stream to the dense region at R.A. = 110°, $d_h = 45$ kpc. There is some evidence for RRab at a greater distance. However, we note that in this region the Sagittarius stream is not very well constrained by our observations. As expected we do observe the trailing stream in the region $0° < \alpha < 80°$. Without any doubt this stream does not continue on the Sgr stream in the region $110° < \alpha < 240°$.

9. DISCUSSION AND CONCLUSIONS

We have presented the initial results of a survey of public CSS data (CSDR1) for RRab's and discovered >12,000 RRab's, of which ∼9400 are newly discovered. The full sample of RRab's ranges in brightness $12.5 < V < 19.5$ and thus reaches heliocentric distances from 3 to 60 kpc. The objects in this catalog generally have average absolute V magnitudes with uncertainties <0.1 mag and periods accurate to better than 0.01%. More than half of the sources have accurate five-color photometry from the SDSS DR8 release and 1531 have SDSS spectra.

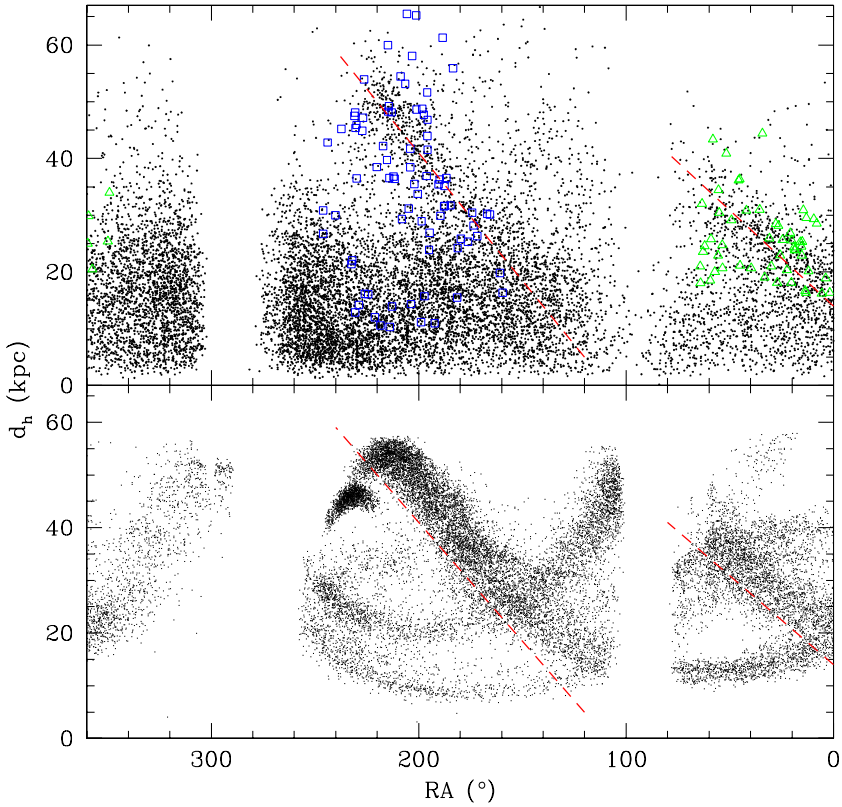

Figure 29. Distribution of RRL distances within the Sgr streams region. Here we have selected RRL and simulated objects in the Sagittarius coordinate system (Majewski et al. 2003) with $-11^\circ < B < 11^\circ$. In the top panel we plot RRab's as well as leading-stream M giants (squares) and trailing-stream M giants (triangles) from LM10. In the lower panel, we plot the LM10 model truncated at 60 kpc after taking into account the CSS survey spatial coverage and extinction. The dashed lines represent the estimates of mean distances of RRab in leading and trailing Sgr arms. These are defined as $d_h = 0.45 \times \delta - 49$ (kpc) and $d_h = 0.338 \times \delta + 14$ (kpc), respectively.

(A color version of this figure is available in the online journal.)

Although this set of RRab's is incomplete within the survey area (because of the magnitude, sampling, and reddening limits of the data), this data set provides a source for more detailed studies of halo streams and structures, as well as a means of constraining the shape, mass, and extent of the Galactic halo (S. E. Koposov et al., in preparation).

Here we provide an initial comparison with models of the Sagittarius stream and find a few discrepancies that should eventually lead to a better understanding of the formation history of the Milky Way halo and its dwarf satellite galaxies. The current data set reaches declinations -22° which extends it $\sim 20^\circ$ beyond the limits of most sources in the SDSS survey. More than 10,000 RRab's have been discovered in photometry from the SSS survey in the region $-75^\circ < \delta < -22^\circ$ (G. Torrealba et al., in preparation). The combination of CSS and SSS RRab's will provide probes of halo structure and Galactic potential covering $\sim 75\%$ of the sky. Additionally, although the MLS survey covers much less area than CSS and SSS, it probes the halo RRLs to distances beyond 100 kpc and has recently confirmed the presence of a distance tidal stream overlapping the Sgr system (Drake et al. 2012).

CRTS and CSDR1 are supported by the U.S. National Science Foundation under grants AST-0909182 and CNS-0540369. The work at Caltech was supported in part by the NASA Fermi grant 08-FERMI08-0025 and by the Ajax Foundation. The CSS survey is funded by the National Aeronautics and Space Administration under grant No. NNG05GF22G issued through the Science Mission Directorate Near-Earth Objects Observations Program. J.L.P. acknowledges support from NASA through Hubble Fellowship grant HF-51261.01-A awarded by the STScI, which is operated by AURA, Inc. for NASA, under contract NAS 5-26555. Support for M.C. and G.T. is provided by the Ministry for the Economy, Development, and Tourism's Programa Inicativa Científica Milenio through grant P07-021-F, awarded to The Milky Way Millennium Nucleus; by Proyecto Basal PFB-06/2007; by Proyecto FONDECYT Regular #1110326; and by Proyecto Anillo ACT-86. SDSS-III is managed by the Astrophysical Research Consortium for the Participating Institutions of the SDSS-III Collaboration. Funding for SDSS-III has been provided by the Alfred P. Sloan Foundation, the Participating Institutions, the National Science Foundation, and the U.S. Department of Energy Office of Science. The SDSS-III Web site is http://www.sdss3.org/. This research has made use of the International Variable Star Index (VSX) database, operated at AAVSO, Cambridge, MA, USA.

REFERENCES

Abazajian, K. F., Adelman-McCarthy, J. K., Agüeros, M. A., et al. 2009, ApJS, 182, 543
Alcock, C., Allsman, R., Alves, D. R., et al. 2000, ApJ, 542, 257
Alcock, C., Alves, D. R., Becker, A., et al. 2003, ApJ, 598, 597
Armosky, B. J., Sneden, C., Langer, G. E., & Kraft, R. P. 1994, AJ, 108, 1364
Azzalini, A. 1985, Scand. J. Stat., 12, 171
Belokurov, V., Evans, N. W., Bell, E. F., et al. 2007, ApJL, 657, 89
Belokurov, V., Zucker, D. B., Evans, N. W., et al. 2006, ApJL, 642, 137

Benedict, G. F., McArthur, B. E., Feast, M. W., et al. 2011, AJ, 142, 187
Bertin, E., & Arnouts, S. 1996, A&AS, 117, 393
Bickerton, S., Badenes, C., Hettinger, T., Beers, T., & Huang, S. 2012, in IAU Symp. 285, New Horizons in Time Domain Astronomy, ed. R. E. M. Griffin, R. J. Hanisch, & R. Seaman (Cambridge: Cambridge Univ. Press), 289
Blazhko, S. 1907, AN, 175, 325
Bono, G., Caputo, F., & Stellingwerf, R. F. 1995, ApJS, 99, 263
Bullock, J. S., Kolatt, T. S., Sigad, Y., et al. 2001, MNRAS, 321, 559
Butler, D. 1975, ApJ, 200, 68
Cacciari, C., Corwin, T. M., & Carney, B. W. 2005, AJ, 129, 267
Casetti-Dinescu, D., Majewski, S. R., Girard, T. M., et al. 2006, AJ, 132, 2082
Casey, A. R., Keller, S. C., & Da Costa, G. 2012, AJ, 143, 88
Catelan, M. 2009, Ap&SS, 320, 261
Catelan, M., & Cortés, C. 2008, ApJL, 676, 135
Chonis, T. S., & Gaskell, C. M. 2007, AJ, 135, 264
Clementini, G., Tosi, M., & Merighi, R. 1991, AJ, 101, 2168
Cohen, J. G., & Melendez, J. 2005, AJ, 129, 303
Cseresnjes, P. 2001, A&A, 375, 909
De Lee, N. 2008, PhD thesis, Michigan State Univ.
Djorgovski, S. G., Drake, A. J., Mahabal, A. A., et al. 2011, in The First Year of *MAXI*: Monitoring Variable X-Ray Sources, ed. T. Mihara & N. Kawai (Tokyo: JAXA Special Publ.)
Drake, A. J., Djorgovski, S. G., Mahabal, A., et al. 2009, ApJ, 696, 870
Drake, A. J., et al. 2012, ApJ, submitted
Eggen, O. J., Lynden-Bell, D., & Sandage, A. R. 1962, ApJ, 136, 748
For, B.-Q., Preston, G. W., & Sneden, C. 2011, ApJS, 197, 29
Freeman, K., & Bland-Hawthorn, J. 2002, ARA&A, 40, 487
Hardie, R. H. 1955, ApJ, 122, 256
Ibata, R. A., Gilmore, G., & Irwin, M. J. 1994, Natur, 370, 194
Ivezic, Z., Smith, J. A., Miknaitis, G., et al. 2007, AJ, 134, 973
Ivezic, Z., Vivas, K., Lupton, R., & Zinn, R. 2005, AJ, 129, 1096
Jurcsik, J., & Kovacs, G. 1996, A&A, 312, 111
Keller, S. C., Murphy, S., Prior, S., Da Costa, G., & Schmidt, B. 2008, ApJ, 678, 851
Kinemuchi, K., Smith, H. A., Woźniak, P. R., et al. 2006, AJ, 132, 1202
Kinman, T. D., & Brown, W. R. 2010, AJ, 139, 2014
Kollmeier, J. S., Gould, A., Shectman, S., et al. 2009, ApJL, 705, 158
Koposov, S. E., Belokurov, V., Evans, N. W., et al. 2012, ApJ, 750, 80
Kraft, R. P., Sneden, C., Langer, G. E., & Prosser, C. F. 1992, AJ, 104, 645
Landolt, A. 2007, AJ, 133, 2502
Landolt, A. 2009, AJ, 137, 4186
Larson, S., Beshore, E., Hill, R., et al. 2003, BAAS, 35, 982
Law, D. R., & Majewski, S. R. 2010, ApJ, 714, 229 (LM10)
Layden, A. C. 1994, AJ, 108, 1016
Lee, Y. S., Beers, T. C., Allende Prieto, C., et al. 2011, AJ, 141, 90
Lee, Y. S., Beers, T. C., Sivarani, T., et al. 2008, AJ, 136, 2022
Lomb, N. R. 1976, Ap&SS, 39, 447
Liu, T. 1991, PASP, 193, 205
Majewski, S., Skrutskie, M. F., Weinberg, M. D., & Ostheimer, J. C. 2003, ApJ, 599, 1082
Mateu, C., Vivas, A. K., Zinn, R., Miller, L. R., & Abad, C. 2009, AJ, 137, 4412
Miceli, A., Rest, A., Stubbs, C. W., et al. 2008, ApJ, 678, 865
Momany, Y., Zaggia, S. R., Bonifacio, P., et al. 2004, A&A, 421, 29
Nemec, J. M. 2004, AJ, 127, 2185
Newberg, H. J., Yanny, B., Cole, N., et al. 2007, ApJ, 668, 221
Newberg, H. J., Yanny, B., Grebel, E. K., et al. 2003, ApJL, 596, 191
Newberg, H. J., Yanny, B., Rockosi, C., et al. 2002, ApJ, 569, 245
Newberg, H. J., Yanny, B., & Willett, B. A. 2009, ApJL, 700, 61
Pietrukowicz, P., Udalski, A., Soszyński, I., et al. 2012, ApJ, 750, 169
Preston, G. W. 1959, AJ, 130, 507
Samus, N. N., Kazarovets, E. V., Pastukhova, E. N., Tsvetkova, T. M., & Durlevich, O. V. 2009, PASP, 121, 1378
Sandage, A. 2004, AJ, 128, 858
Sandstrom, K., Pilachowski, C. A., & Saha, A. 2001, AJ, 122, 3212
Scargle, J. D. 1982, ApJ, 263, 835
Schlegel, D. J., Finkbeiner, D. P., & Davis, M. 1998, ApJ, 500, 525
Schwarzenberg-Czerny, A. 1989, MNRAS, 241, 153
Schwarzenberg-Czerny, A. 1996, ApJL, 460, 107
Schwarzenberg-Czerny, A. 1998, MNRAS, 301, 831
Searle, L., & Zinn, R. 1978, ApJ, 225, 357
Sesar, B. 2012, AJ, 144, 114
Sesar, B., Ivezić, Ž., Grammer, S. H., et al. 2010, ApJ, 708, 717
Sesar, B., Ivezić, Ž., Lupton, R. H., et al. 2007, AJ, 134, 2236
Sirko, E., Goodman, J., Knapp, G. R., et al. 2004, AJ, 127, 899
Skrutskie, M. F., Cutri, R. M., Stiening, R., et al. 2006, AJ, 131, 1163
Smith, H. A., Catelan, M., & Kuehn, C. 2011, in RR Lyrae Stars, Metal-Poor Stars, and the Galaxy, ed. A. McWilliam (Carnegie Observatories Series, Vol. 5; Pasadena, CA: The Observatories of the Carnegie Institution of Washington), 17
Soszyński, A., Udalski, A., Szymański, M. K., et al. 2009, AcA, 59, 1
Stetson, P. B. 2000, PASP, 112, 925
Stetson, P. B. 2005, PASP, 117, 563
Szczygiel, D. M., Pojmanski, G., & Pilecki, B. 2009, AcA, 59, 137
Vivas, A. K., Jaffé, Y. L., Zinn, R., et al. 2008, AJ, 136, 1645
Vivas, A. K., & Zinn, R. 2006, AJ, 132, 714
Vivas, A. K., Zinn, R., Abad, C., et al. 2004, AJ, 127, 1158
Vivas, A. K., Zinn, R., & Gallart, C. 2005, AJ, 129, 189
Watkins, L. L., Evans, N. W., Belokurov, V., et al. 2009, MNRAS, 398, 1757
Watson, C., Henden, A. A., & Price, A. 2006, SASS, 25, 47
Welch, D. L., & Stetson, P. B. 1993, AJ, 105, 1813
Yanny, B., Rockosi, C., Newberg, H. J., et al. 2009, AJ, 137, 4377
Zinn, R., & West, M. J. 1984, ApJS, 55, 45
Zorotovic, M., Catelan, M., Smith, H. A., et al. 2010, AJ, 139, 357